JPL Publication 11-5

HyspIRI Level-2 Thermal Infrared (TIR) Land Surface Temperature and Emissivity Algorithm Theoretical Basis Document

G. Hulley
S. Hook
Jet Propulsion Laboratory

National Aeronautics and Space Administration

Jet Propulsion Laboratory
California Institute of Technology
Pasadena, California

May 2011

This research was carried out at the Jet Propulsion Laboratory, California Institute of Technology, under a contract with the National Aeronautics and Space Administration.

Revisions:

Version 1.0 draft by Glynn Hulley, 09/26/2011

Contacts

Readers seeking additional information about this study may contact the following researchers:

Glynn C. Hulley
MS 183-501
Jet Propulsion Laboratory
4800 Oak Grove Dr.
Pasadena, CA 91109
Email: glynn.hulley@jpl.nasa.gov
Office: (818) 354-2979

Simon J. Hook
MS 183-501
Jet Propulsion Laboratory
4800 Oak Grove Dr.
Pasadena, CA 91109
Email: simon.j.hook@jpl.nasa.gov
Office: (818) 354-0974

Abstract

The Hyperspectral Infrared Imager (HyspIRI) satellite includes a thermal infrared (TIR) multispectral scanner with seven spectral bands in the thermal infrared (TIR) between 7 and 12 µm and one band in the mid-infrared between 3 and 5 µm designed to measure hot targets. The TIR bands have a NEΔT of <0.2 K at 300K and all bands have a spatial scale of 60 m. The two primary Level-2 products that will be generated by HyspIRI TIR data are surface temperature and emissivity. Both of these products will be generated from the six spectral bands between 8 and 12 µm (Bands 2-6). The first band around 4 µm is designed for measuring hot targets and a different algorithm will be used to recover temperatures from it. The second band around 7.5 µm will be used to help with atmospheric correction. The surface radiance emitted from the Earth's surface depends on both temperature and emissivity, and separating these two components from the total radiance is difficult because there are more unknowns than there are measurements, presenting an ill-posed problem. For example, with the six HyspIRI TIR bands between 8 and 12 µm, there will be six measurements and seven unknowns (six band emissivities and one temperature). Various approaches have been proposed to solve this ill-posed problem. One such approach, developed for ASTER on NASA's Terra platform, is termed the Temperature Emissivity Separation (TES) algorithm. Inputs to TES include the surface radiance, which is determined from atmospherically correcting the at-sensor radiance for path radiance and atmospheric absorption and the sky irradiance. TES is a hybridization of two previously well-established algorithms: the normalized emissivity method (NEM) and the alpha residual method. First, emissivities and temperature are estimated with the NEM method, while using an iterative approach to remove downwelling sky irradiance. Next, the NEM emissivities are normalized by their mean. An empirical relationship based on the alpha residual method is then used to estimate the minimum emissivity, given the spectral contrast, or min-max differences (MMD), by using a calibration curve determined from laboratory measurements. Limitations in TES arise due to the empirical constraint the minimum emissivity and MMD, measurement accuracy, calibration, atmospheric correction, and removal of the reflected component of downwelling radiation. Previous studies have demonstrated that together these limitations result in a typical temperature uncertainty in of 1.5 K but the exact uncertainty will depend on the surface and atmospheric conditions at the time of the retrieval.

Contents

Figures

Tables

1 Introduction

The Hyperspectral Infrared Imager (HyspIRI) mission includes two instruments: a visible shortwave infrared (VSWIR) imaging spectrometer operating between 380 and 2500 nm in 10-nm contiguous bands and a thermal infrared (TIR) multispectral scanner with eight spectral bands operating between 4 and 12 µm. Both instruments acquire data with a spatial resolution of 60m from the nominal orbit altitude. The VSWIR and TIR instruments have revisit times of 19 and 5 days with swath widths of 145 and 600 km, respectively.

This document outlines the theory and methodology for generating the HyspIRI TIR Level-2 land surface temperature and emissivity (LST&E) products. These products are derived from the six TIR spectral bands between 8 and 12 µm. A separate approach will be used to recover the temperature from the first spectral band in the mid infrared (MIR) between 3 and 5 µm which is designed to measure the temperature of very hot targets (up to 1200 K). The second band around 7.5 µm is used to aid with the atmospheric correction. The LST&E are derived from the surface radiance that is obtained by atmospherically correcting the at-sensor radiance.. LST&E products are essential for a wide range of Earth system studies. For example, emissivity spectral signatures are important for geologic studies and mineral mapping studies (Hook et al. 2005; Vaughan et al. 2005). This is because emissivity features in the TIR region are unique for many different types of materials that make up the Earth's surface, for example, quartz, which is ubiquitous in most of the arid regions of the world.. Emissivities are also used for land use and land cover change mapping since vegetation fractions can often be inferred if the background soil is observable (French et al. 2008). Knowledge of the surface emissivity is also critical for accurately recovering the surface temperature, a key climate variable in many scientific studies from climatology to hydrology, modeling the greenhouse effect, drought monitoring, and surface energy balance studies (Anderson et al. 2007; French et al. 2005; Jin and Dickinson 2010).

The HyspIRI TIR measurement derives its heritage from the ASTER measurement. ASTER is a five-channel multispectral TIR scanner that was launched on NASA's Terra spacecraft in Dec. 1999 with a 90-m spatial resolution and revisit time of 16 days. The HyspIRI LST&E products will be produced globally over all land cover types, excluding open oceans for all cloud-free pixels. Generation of the LST&E products will be undertaken as part of the HyspIRI Project activities It is anticipated that these products will be merged to produce weekly, monthly, and seasonal products, with the monthly product most likely producing global

coverage, depending on cloud coverage, however, the generation of these higher level merged products is not considered to be a Project activity. The Level 2 products will be validated with a mean ASTER seasonal emissivity map (e.g., summertime - July, Aug., Sept.) termed the North American ASTER Land Surface Emissivity Database (NAALSED), which was generated for North America using all available ASTER data over a 10-year period (Hulley and Hook 2009b). By contrast, HyspIRI will have the capability to produce such a product in less than one month. Because HyspIRI will have similar band placements and spatial footprint as ASTER, this type of comparison will be useful as a preliminary assessment of the accuracy of the LST&E products.

Maximum radiometric emission for the typical range of Earth surface temperatures, excluding fires and volcanoes, is found in two infrared spectral "window" regions: the midwave infrared (3.5–5 μm) and the thermal infrared (8–13 μm). The radiation emitted in these windows for a given wavelength is a function of both temperature and emissivity. Determining the separate contribution from each component in a radiometric measurement is an ill-posed problem since there will always be more unknowns—N emissivities and a single temperature—than the number of measurements, N, available. For HyspIRI, we will be solving for one temperature and six emissivities (HyspIRI TIR bands 3–8). Therefore, an additional constraint is needed, independent of the data. There have been numerous theories and approaches over the past two decades to solve for this extra degree of freedom. For example, the ASTER Temperature Emissivity Working Group (TEWG) analyzed ten different algorithms for solving the problem (Gillespie et al. 1999). Most of these relied on a radiative transfer model to correct at-sensor radiance to surface radiance and an emissivity model to separate temperature and emissivity. Other approaches include the split-window (SW) algorithm, which extends the SST SW approach to land surfaces, assuming that land emissivities in the window region (10.5–12 μm) are stable and well known. However, this assumption leads to unreasonably large errors over barren regions where emissivities have large variations both spatially and spectrally. The ASTER TEWG finally decided on a hybrid algorithm, termed the temperature emissivity separation (TES) algorithm, which capitalizes on the strengths of previous algorithms with additional features (Gillespie et al. 1998).

TES is applied to the land-leaving TIR radiances that are estimated by atmospherically correcting the at-sensor radiance on a pixel-by-pixel basis using a radiative transfer model. The methodology to atmospherically correct the TIR radiances is described in the HyspIRI Level 2

Surface Radiance ATBD . TES uses an empirical relationship to predict the minimum emissivity that would be observed from a given spectral contrast, or minimum-maximum difference (MMD) (Kealy and Hook 1993; Matsunaga 1994). The empirical relationship is referred to as the calibration curve and is derived from a subset of spectra in the ASTER spectral library (Baldridge et al. 2009). A new calibration curve, applicable to HyspIRI TIR bands, will be computed with an updated version of the ASTER spectral library, termed the HyspIRI spectral library, which will consist of all original spectra resampled to the HyspIRI VSWIR and TIR instrument spectral characteristics. TES has been shown to accurately recover temperatures within 1.5 K and emissivities within 0.015 for a wide range of surfaces and is a well established physical algorithm that produces seamless images with no artificial discontinuities such as might be seen in a land classification type algorithm (Gillespie et al. 1998).

The remainder of the document will discuss the HyspIRI instrument characteristics, provide a background on TIR remote sensing, give a full description and background on the TES algorithm, provide quality assessment, discuss numerical simulation studies and, finally, outline a validation plan.

2 HyspIRI Instrument Characteristics

The TIR instrument will acquire data in eight spectral bands, seven of which are located in the thermal infrared part of the electromagnetic spectrum between 7 and 13 µm shown in Figure 1; the remaining band is located in the mid infrared part of the spectrum around 4 µm. The center position and width of each band is provided in Table 1. The exact spectral location of each band has not been determined, the nominal locations provided here are based on the measurement requirements identified in the science-traceability matrices, which included recognition that related data was acquired by other sensors such as ASTER and MODIS. HyspIRI will contribute to maintaining a longtime series of these measurements. For example, the positions of three of the TIR bands closely match the first three thermal bands of ASTER, while two of the TIR bands match bands of ASTER and MODIS typically used for split-window type applications (ASTER bands 12–14 and MODIS bands 31, 32). It is expected that small adjustments to the band positions will be made based on ongoing science activities.

A key science objective for the TIR instrument is the study of hot targets (volcanoes and wildfires), so the saturation temperature for the 4-µm channel is set high (1200 K), whereas the saturation temperatures for the thermal infrared channels are set at 500 K.

The TIR instrument will operate as a whiskbroom mapper, similar to MODIS but with 256 pixels in the cross-whisk direction for each spectral channel (Figure 2). A conceptual layout for the instrument is shown in Figure 3. The scan mirror rotates at a constant angular speed. It sweeps the focal plane image across nadir, then to a blackbody target and space, with a 2.2-second cycle time.

The f/2 optics design is all reflective, with gold-coated mirrors. The 60-K focal plane will be single-bandgap mercury cadmium telluride (HgCdTe) detector, hybridized to a CMOS readout chip, with a butcher block spectral filter assembly over the detectors. Thirty-two analog output lines, each operating at 10–12.5 MHz, will move the data to analog-to-digital converters.

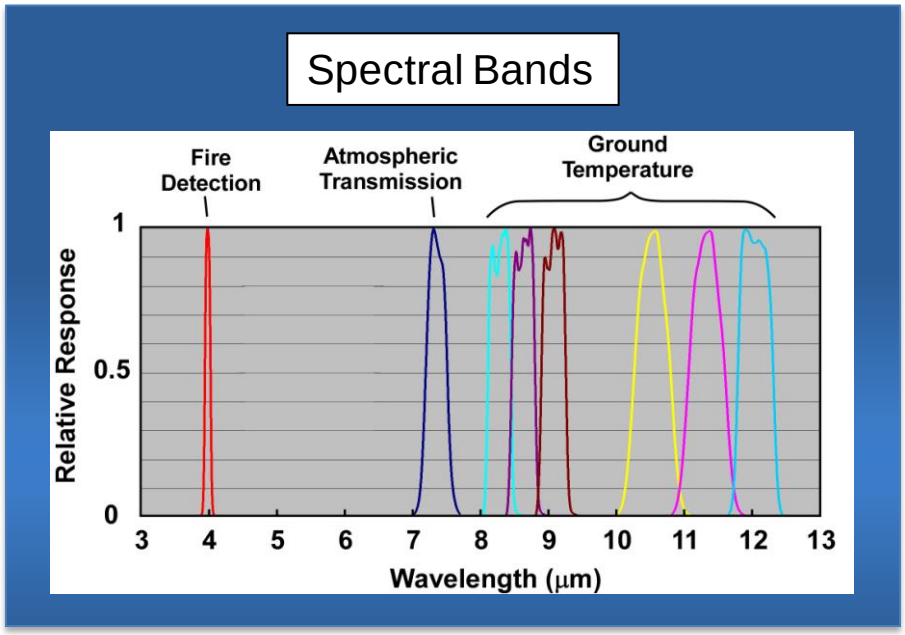

Figure 1: HyspIRI TIR instrument proposed spectral bands.

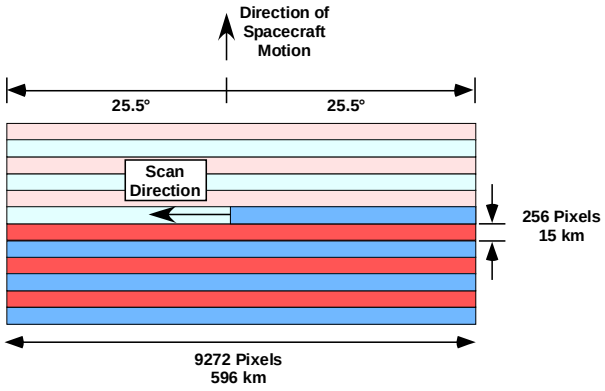

Figure 2: HyspIRI TIR scanning scheme.

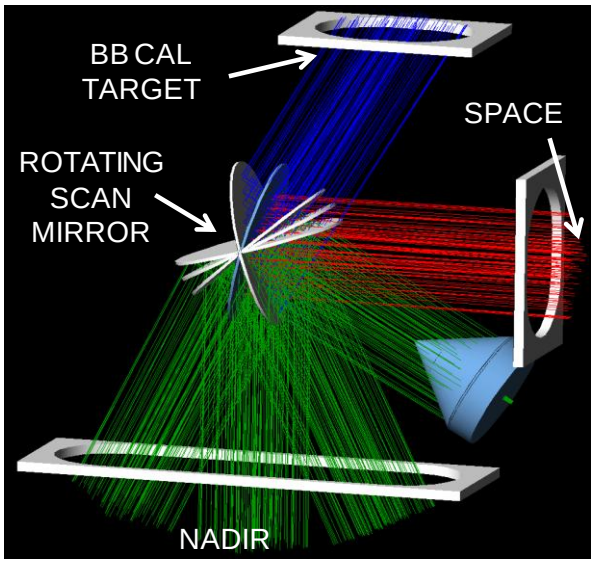

Figure 3: HyspIRI TIR conceptual layout.

The temperature resolution of the thermal channels is much finer than the mid-infrared channel, which (due to its high saturation temperature) will not detect a strong signal until the target is above typical terrestrial temperatures at around 400K. All the TIR channels are quantized at 14 bits. Expected sensitivities of the eight channels, expressed in terms on noise-equivalent temperature difference, are shown in the following two plots (Figures 4 and 5).

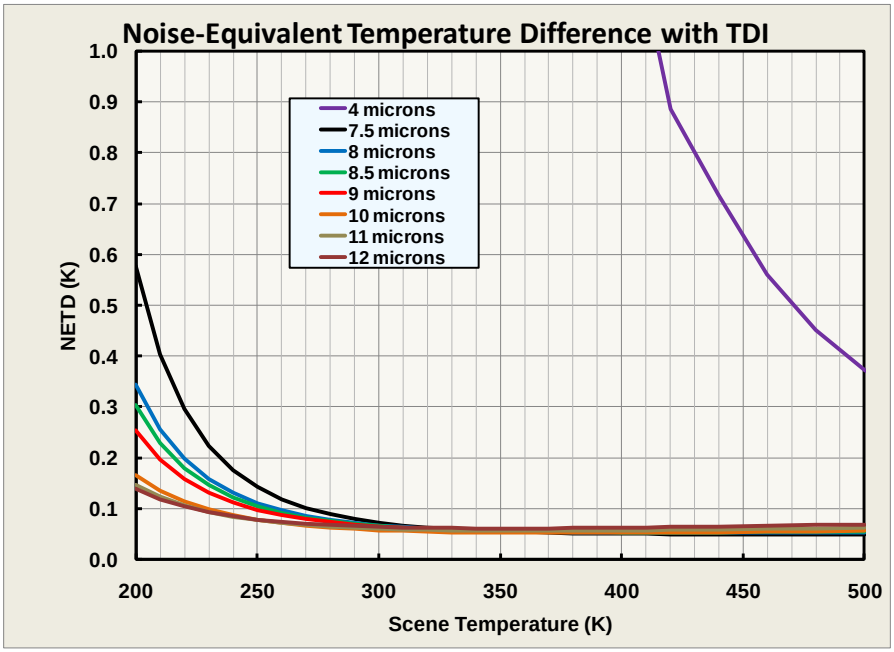

Figure 4: HyspIRI TIR predicted sensitivity 200–500 K.

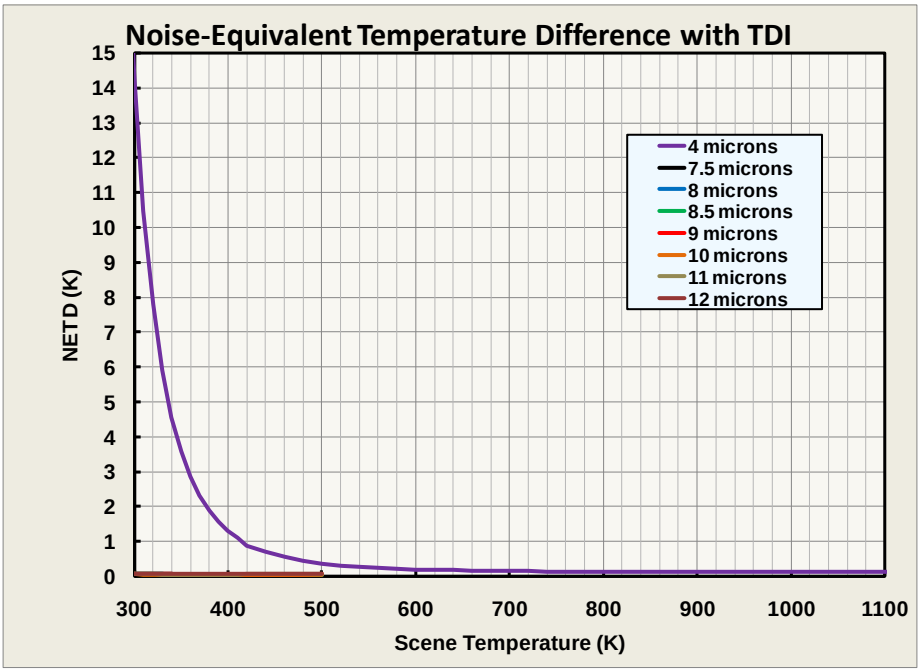

Figure 5: HyspIRI TIR predicted sensitivity 300–1100 K.

The TIR instrument will have a swath width of 600 km with a pixel spatial resolution of 60 m, resulting in a temporal revisit of 5 days at the equator. The instrument will be on both day and night, and it will acquire data over the entire surface of the Earth. Like the VSWIR, the TIR instrument will acquire full spatial resolution data over the land and coastal oceans (to a depth of

<50 m) but, over the open oceans, the data will be averaged to a spatial resolution of 1 km. The large swath width of the TIR will enable multiple revisits of any spot on the Earth every week (at least 1 day view and 1 night view). This repeat period is necessary to enable monitoring of dynamic or cyclical events such as volcanic hotspots or crop stress associated with water availability.

Table 1: Preliminary TIR Measurement Characteristics

Spectral	
Bands (8) µm	3.98 µm, 7.35 µm, 8.28 µm, 8.63 µm, 9.07 µm, 10.53 µm, 11.33 µm, 12.05 µm
Bandwidth	0.084 µm, 0.32 µm, 0.34 µm, 0.35 µm, 0.36 µm, 0.54 µm, 0.54 µm, 0.52 µm
Accuracy	<0.01 µm
Radiometric	
Range	Bands 2–8 = 200 K – 500 K; Band 1 = 1200 K
Resolution	< 0.05 K, linear quantization to 14 bits
Accuracy	< 0.5 K 3-sigma at 250 K
Precision (NEdT)	< 0.2 K
Linearity	>99% characterized to 0.1 %
Spatial	
IFOV	60 m at nadir
MTF	>0.65 at FNy
Scan Type	Push-Whisk
Swath Width	600 km (±25.5° at 623-km altitude)
Cross Track Samples	9,300
Swath Length	15.4 km (± 0.7 degrees at 623 km altitude)
Down Track Samples	256
Band to Band Co-Registration	0.2 pixels (12 m)
Pointing Knowledge	10 arcsec (0.5 pixels) (approximate value, currently under evaluation)
Temporal	
Orbit Crossing	11 a.m. Sun synchronous descending
Global Land Repeat	5 days at Equator
On Orbit Calibration	
Lunar views	1 per month {radiometric}
Blackbody views	1 per scan {radiometric}
Deep Space views	1 per scan {radiometric}
Surface Cal Experiments	2 (day/night) every 5 days {radiometric}
Spectral Surface Cal Experiments	1 per year
Data Collection	
Time Coverage	Day and Night
Land Coverage	Land surface above sea level
Water Coverage	Coastal zone minus 50 m and shallower
Open Ocean	Averaged to 1-km spatial sampling
Compression	2:1 lossless

3 Science Objectives

The HyspIRI mission is science driven by linking the measurement requirements for the mission to one or more science questions. HyspIRI has three top-level science questions related to 1) ecosystem function and composition, 2) volcanoes and natural hazards, and 3) surface composition and the sustainable management of natural resources (HyspIRI 2008). The NRC Decadal Survey called out these three areas. These questions provide a scientific framework for the HyspIRI mission. NASA appointed the HyspIRI Science Study Group (SSG) to refine and expand these questions to a level of detail that was sufficient to define the measurement requirements for the HyspIRI mission.

Five overarching thematic questions were defined by the HyspIRI SSG for the TIR component, as follows:

- TQ1: **Volcanoes and Earthquakes**: How can we help predict and mitigate earthquake and volcanic hazards through detection of transient thermal phenomena?
- TQ1: **Wildfires**: What is the impact of global biomass burning on the terrestrial biosphere and atmosphere, and how is this impact changing over time?
- TQ3: **Water Use and Availability**: How is consumptive use of global freshwater supplies responding to changes in climate and demand, and what are the implications for sustaining water resources?
- TQ4: **Urbanization and Human Health**: How does urbanization affect the local, regional, and global environment? Can we characterize this effect to help mitigate its effects on human health and welfare?

- TQ5: **Earth Surface Composition and Change**: What is the composition and thermal properties of the exposed surface of the Earth? How do these factors change over time and affect land use and its habitability?

For each of these questions, accurate retrieval of LST&E plays a key role in defining the measurement objectives and requirements for these questions. The HyspIRI LST product, in particular, will be especially useful for studies of surface energy and water balance in agricultural regions at the crop scale (<100 m), where quantification of evapotranspiration processes are essential for helping land managers make important decisions relating to water use and availability. The HyspIRI emissivity product will contain information from rocks, soils, and vegetation at different wavelengths, which will provide a diagnostic tool for discriminating surface cover types at fine spatial scales.

4 Theory and Methodology

4.1 TIR Remote-Sensing Background

The at-sensor measured radiance in the TIR spectral region (8–14 μm) is a combination of different terms from surface emission and the atmosphere. The Earth-emitted radiance is a function of temperature and emissivity and gets attenuated by the atmosphere on its path to the satellite. The atmosphere also emits radiation, of which some reaches the sensor directly as "path radiance," while some gets radiated to the surface (irradiance) and reflected back to the sensor, commonly known as the reflected downwelling sky irradiance. One effect of the sky irradiance is the reduction of the spectral contrast of the emitted radiance, due to Kirchhoff's law. Assuming the spectral variation in emissivity is small (Lambertian assumption), and using Kirchhoff's law to express the hemispherical-directional reflectance as directional emissivity ($\rho_\lambda = 1 - \epsilon_\lambda$), the

clear sky at-sensor radiance can be written as three terms: the Earth-emitted radiance described by Planck's function and reduced by the emissivity factor, ϵ_λ; the reflected downwelling irradiance; and the path radiance.

$$L_\lambda(\theta) = \left[\epsilon_\lambda B_\lambda(T_s) + (1-\epsilon_\lambda)L_\lambda^{\downarrow}\right]\tau_\lambda(\theta) + L_\lambda^{\uparrow}(\theta) \quad (1)$$

$L_\lambda(\theta)$ = at-sensor radiance;

λ = wavelength;

θ = observation angle;

ϵ_λ = surface emissivity;

T_s = surface temperature;

$L_\lambda^{\downarrow}$ = downwelling sky irradiance;

$\tau_\lambda(\theta)$ = atmospheric transmittance;

$L_\lambda^{\uparrow}(\theta)$ = atmospheric path radiance

$B_\lambda(T_s)$ = Planck function, described by Planck's law:

$$B_\lambda = \frac{c_1}{\pi\lambda^5}\left(\frac{1}{\exp\left(\frac{c_2}{\lambda T}\right)-1}\right) \quad (2)$$

$c_1 = 2\pi hc^2$=3.74· 10^{-16} W·m^2 (1st radiation constant)

h = 6.63· 10^{-34} W·s^2 (Planck's constant)

c2 = h·c/k = 1.44× 10^4 µm·K (2nd radiation constant)

k = 1.38× 10^{-23} W·s·K^{-1} (Boltzmann's constant)

c = 2.99· 10^8 m·s^{-1} (speed of light)

Figure 6 shows the relative contributions from the surface-emission term, surface radiance, and at-sensor radiance for a US Standard Atmosphere, quartz emissivity spectrum, and surface temperature set to 300 K. Vertical bars show the placement of the eight HyspIRI MWIR and TIR bands. The reflected downwelling term adds a small contribution in the window regions but will become more significant for more humid atmospheres. The at-sensor radiance shows large departures from the surface radiance in regions where atmospheric absorption from gases such as CO_2, H_2O, and O_3 are high.

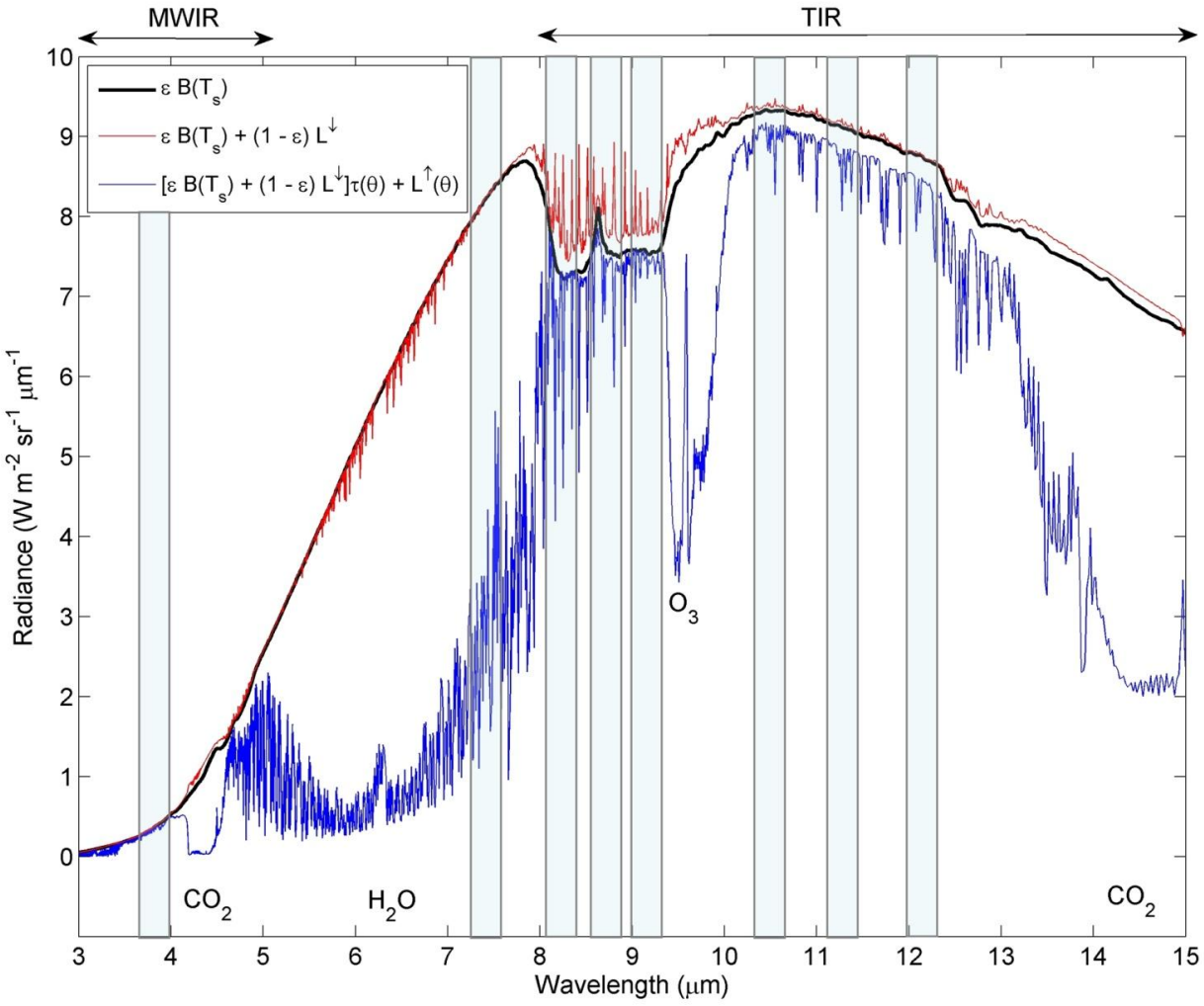

Figure 6: Radiance simulations of the surface-emitted radiance, surface-emitted and reflected radiance, and at-sensor radiance using the MODTRAN 5.2 radiative transfer code, US Standard Atmosphere, quartz emissivity spectrum, surface temperature = 300K, and viewing angle set to nadir. Vertical bars show placements of the HyspIRI MWIR and TIR bands.

Equation (1) gives the at-sensor radiance for a single wavelength, λ, while the measurement from a sensor is typically measured over a range of wavelengths, or band. The at-sensor radiance for a discrete band, i, is obtained by weighting and normalizing the at-sensor spectral radiance calculated by equation (1) with the sensor's spectral response function for each band, Sr_λ, as follows:

$$L_i(\theta) = \frac{\int Sr_\lambda(\mathrm{i}) \cdot L_\lambda(\theta) \cdot \mathrm{d}\lambda}{Sr_\lambda(\mathrm{i}) \cdot \mathrm{d}\lambda} \tag{3}$$

Using equations (1) and (2), the surface radiance for band i can be written as a combination of two terms: Earth-emitted radiance, and reflected downward irradiance from the sky and surroundings:

$$L_{s,i} = \epsilon_i B_i(T_s) + (1-\epsilon_i)L_i^{\downarrow} = \frac{L_i(\theta) - L_i^{\uparrow}(\theta)}{\tau_i(\theta)} \tag{4}$$

The atmospheric parameters, $L_\lambda^{\downarrow}$, $\tau_\lambda(\theta)$, $L_\lambda^{\uparrow}(\theta)$, are estimated with a radiative transfer model such as MODTRAN (Kneizys et al. 1996) using input atmospheric fields of air temperature, relative humidity, and geopotential height.

The emissivity of an isothermal, homogeneous emitter is defined as the ratio of the actual emitted radiance to the radiance emitted from a black body at the same thermodynamic temperature (Norman and Becker 1995), $\epsilon_\lambda = R_\lambda / B_\lambda$. The emissivity is an intrinsic property of the Earth's surface and is an independent measurement of the surface temperature, which varies with irradiance and local atmospheric conditions. The emissivity of most natural Earth surfaces for the TIR wavelength ranges between 8 and 12 μm and, for a sensor with spatial scales <100 m, varies from ~0.7 to close to 1.0. Narrowband emissivities less than 0.85 are typical for most desert and semi-arid areas due to the strong quartz absorption feature (reststrahlen band) between

the 8- and 9.5-μm range, whereas the emissivity of vegetation, water, and ice cover are generally greater than 0.95 and spectrally flat in the 8–12-μm range.

*** More here to be added in the future of typical radiance values using MODTRAN (give table for different atmospheres and conditions).

4.2 Temperature and Emissivity Separation Approaches

The radiance in the TIR atmospheric window (8–13 μm) is dependent on the temperature and emissivity of the surface being observed. Even if the atmospheric properties (water vapor and air temperature) are well known and can be removed from equation (1), the problem of retrieving surface temperature and emissivity from multispectral measurements is still a non-deterministic process. This is because the total number of measurements available (N bands) is always less than the number of variables to be solved for (emissivity in N bands and one surface temperature). Therefore, no retrieval will ever do a perfect job of separation, with the consequence that errors in temperature and emissivity may co-vary. If the surface can be approximated as Lambertian (isotropic) and the emissivity is assigned *a priori* from a land cover classification, then the problem becomes deterministic with only the surface temperature being the unknown variable. Examples of such cases would be over ocean, ice, or densely vegetated scenes where the emissivity is known and spectrally flat in all bands. Another deterministic approach is the single-band inversion approach. If the atmospheric parameters are known in equation (1), then the temperature can also be solved for using a single band, usually in the clearest region of the window (~11 μm). Deterministic approaches are usually employed with sensors that have two or three bands in the TIR region, while non-deterministic approaches are applied to multispectral sensors so that spectral variations in the retrieved emissivity can be related to surface composition and cover, in addition to retrieving the surface temperature. For HyspIRI, a non-deterministic approach will be used, as spectral emissivity will need to be determined physically, along with temperature, in order to help answer the science questions outlined previously in section 3.

4.2.1 Deterministic Approaches

4.2.1.1 Split-window Algorithms

The most common deterministic approach can be employed without having to explicitly solve the radiative transfer equation. Two or more bands are employed in the window region (typically 10.5–12 μm), and atmospheric effects are compensated for by the differential absorption characteristics from the two bands. This approach is used with much success over oceans to compute the SST (Brown and Minnett 1999), as the emissivity of water is well known (Masuda et al. 1988). Variations of this method over land include the split-window (SW) approach (Coll and Caselles 1997; Prata 1994; Price 1984; Wan and Dozier 1996; Yu et al. 2008), the multichannel algorithm (Deschamps and Phulpin 1980), and the dual-angle algorithm (Barton et al. 1989). Over land, the assumption is that emissivities in the split-window bands being used are stable and well known and can be assigned using a land cover classification map (Snyder et al. 1998). However, this assumption introduces large errors over barren surfaces where much larger variations in emissivity are found due to the presence of large amounts of exposed rock or soil often with abundant silicates (Hulley and Hook 2009a). Land cover classification maps typically use VNIR data for assignment of various classes. This method may work for most vegetation types and over water surfaces but, because VNIR reflectances correspond predominately to Fe oxides and OH^- and not to the Si-O bond over barren areas, there is little or no correlation with silicate mineralogy features in thermal infrared data. This is why, in most classification maps, only one bare land class is specified (barren). This type of approach will not be used for the HyspIRI standard algorithm for the following reasons:

1. One of the goals of HyspIRI TIR science is to retrieve the spectral emissivity of geologic surfaces for compositional analysis. Classification does not produce this type of product.

2. The emissivity of the land surface is in general heterogeneous and is dependent on many factors including surface soil moisture, vegetation cover changes, and surface compositional changes, which are not characterized by classification maps.
3. Split-window algorithms are inherently very sensitive to measurement noise between bands.
4. Classification leads to sharp discontinuities and contours in the data between different class types. This violates one of the goals of HyspIRI in producing seamless images.
5. Temperature inaccuracies are difficult to quantify over geologic surfaces where constant emissivities are assigned.

4.2.1.2 Single-band Inversion

If the atmosphere is known, along with an estimate of the emissivity, then equation (1) can be inverted to retrieve the surface temperature using one band. Theoretically, any band used should retrieve the same temperature, but uncertainties in the atmospheric correction will result in subtle differences as different bands have stronger atmospheric absorption features than others which may be imperfectly corrected for atmospheric absorption. For example, a band near 8 μm will have larger dependence on water vapor, while the 9–10-μm region will be more susceptible to ozone absorption. Jimenez-Munoz and Sobrino (2010) applied this method to ASTER data by using atmospheric functions (AFs) to account for atmospheric effects. The AFs can be computed by the radiative transfer equation or empirically given the total water vapor content. The clearest ASTER band (13 or 14) was used to retrieve the temperature, with the emissivity determined using an NDVI fractional vegetation cover approach. A similar procedure has been proposed to retrieve temperatures from the Landsat TIR band 6 on ETM+ and TM sensors (Li et al. 2004). The single-band inversion method will not be used for HyspIRI for the following reasons:

1. One of the goals of HyspIRI science will be to retrieve the spectral emissivity of geologic surfaces for compositional analysis. This will not be possible with the single-band approach, which assigns emissivity based on land cover type and vegetation fraction.
2. Estimating emissivity from NDVI-derived vegetation cover fraction over arid and semi-arid regions will introduce errors in the LST because NDVI is responsive only to chlorophyll active vegetation, and does not correlate well with senescent vegetation (e.g., shrublands).
3. Only one-band emissivity is solved for the single-band inversion approach. HyspIRI will be a multispectral retrieval approach.

4.2.2 Non-deterministic Approaches

In non-deterministic approaches, the temperature and emissivity is solved using an additional constraint or extra degree of freedom that is independent of the data source. These types of solutions are also rarely perfect because the additional constraint will always introduce an additional level of uncertainty, however, they work well over all surfaces (including arid and semi arid) and can automatically account for changes in the surface e.g. due to fire or moisture. First, we introduce two well-known approaches, the day/night and TISI algorithms, followed by an examination of the algorithms and methods that led up to establishment of the TES algorithm.

4.2.2.1 Day/Night Algorithm

The constraint in the day/night algorithm capitalizes on the fact that the emissivity is an intrinsic property of the surface and should not change from day- to nighttime observations. The day/night algorithm is currently used to retrieve temperature/emissivity from MODIS data in the MOD11B1 product (Wan and Li 1997). The method relies on two measurements (day and night), and the theory is as follows: Two observations in N bands produces 2N observations, with the unknown variables being N-band emissivities, a day- and nighttime surface temperature, four

atmospheric variables (day and night air temperature and water vapor), and an anisotropic factor, giving N + 7 variables. In order to make the problem deterministic, the following conditions must be met: $2N \geq N+7$, or $N \geq 7$. For the MODIS algorithm, this can be satisfied by using bands 20, 22, 23, 29, 31–33. Although this method is theoretically sound, the retrieval is complicated by the fact that two clear, independent observations are needed (preferably close in time) and the pixels from day and night should be perfectly co-registered. Errors may be introduced when the emissivity changes from day to night observation (e.g., due to condensation or dew), and from undetected nighttime cloud. In addition, the method relies on very precise co-registration between the day- and nighttime pixel.

4.2.2.2 Temperature Emissivity Separation Approaches

During research activities leading up to the ASTER mission, the ASTER Temperature Emissivity Working Group (TEWG) was established in order to examine the performance of existing non-deterministic algorithms and select one suitable for retrieving the most accurate temperature and/or emissivity over the entire range of terrestrial surfaces. This lead to development of the TES algorithm, which ended up being a hybrid algorithm that capitalized on the strengths of previous algorithms. In Gillespie et al. (1999), ten inversion algorithms were outlined and tested, leading up to development of TES. For all ten algorithms, an independent atmospheric correction was necessary. The ten algorithms were as follows:

1. Alpha-derived emissivity (ADE) method
2. Classification method
3. Day-Night measurement
4. Emissivity bounds method

5. Graybody emissivity method
6. Mean-MMD method (MMD)
7. Model emissivity method
8. Normalized emissivity method (NEM)
9. Ratio Algorithm
10. Split-window algorithm

In this document, we will briefly discuss a few of the algorithms but will not expand upon any of them in great detail. The day-night measurement (3), classification (2), and split-window (10) algorithms have already been discussed in section 4.2.1. A detailed description of all ten algorithms is available in Gillespie et al. (1999). The various constraints proposed in these algorithms either determine spectral shape but not temperature, use multiple observations (day and night), assume a value for emissivity and calculate temperature, assume a spectral shape, or assume a relationship between spectral shape and minimum emissivity.

The normalized emissivity method (NEM) removes the downwelling sky irradiance component by assuming an ϵ_{max} of 0.99. Temperature is then estimated by inverting the Planck function and a new emissivity found. This process is repeated until successive changes in the estimated surface radiances are small. This method in itself was not found to be suitable for ASTER because temperature inaccuracies tended to be high (>3 K) and the emissivities had incorrect spectral shapes. Other approaches have used a model to estimate emissivity at one wavelength (Lyon 1965) or required that the emissivity be the same at two wavelengths (Barducci and Pippi 1996). This introduces problems for multispectral data with more than 5 bands, e.g., ASTER or HyspIRI.

The ADE method (Hook et al. 1992; Kealy et al. 1990; Kealy and Hook 1993) is based on the alpha residual method that preserves emissivity spectral shape but not amplitude or temperature. The constraint introduced uses an empirical relationship between spectral contrast and average emissivity to restore the amplitude of the alpha-residual spectrum and to compute temperature. The average emissivity was used in the relationship to minimize band-to-band calibration errors. The TEWG used this key feature of the ADE method in TES, although the minimum emissivity instead of average emissivity was used in the empirical relationship (Matsunaga 1994). The ADE itself was not fully employed for two primary reasons as discussed in Gillespie et al. (1999): 1) ADE uses Wien's approximation, exp(x) - 1 = exp(x), which introduces a noticeable "tilt" in the residual spectra that gets transferred to the final emissivity spectra; and 2) This issue was easily fixed in the hybrid version of TES.

Lastly, the temperature-independent spectral indices (TISI) approach (Becker and Li 1990) computes relative emissivities from power-scaled brightness temperatures. TISI, however, is band-dependent and only recovers spectral shape; furthermore, the values are non unique. To retrieve actual emissivities, additional information or assumptions are needed. Other algorithms, which only retrieve spectral shape, are the thermal log and alpha residual approach (Hook et al. 1992) and spectral emissivity ratios (Watson 1992; Watson et al. 1990). Neither of these were considered because they do not recover temperature or actual emissivity values.

5 Temperature Emissivity Separation (TES) Algorithm

The final TES algorithm proposed by the ASTER TEWG combined some core features from previous algorithms and, at the same time, improved on them. TES combines the NEM, the ratio, and the minimum-maximum difference (MMD) algorithm to retrieve temperature and a full emissivity spectrum. The NEM algorithm is used to estimate temperature and iteratively

remove the sky irradiance, from which an emissivity spectrum is calculated, and then ratioed to their mean value in the ratio algorithm. At this point, only the shape of the emissivity spectrum is preserved, but not the amplitude. In order to compute an accurate temperature, the correct amplitude is then found by relating the minimum emissivity to the spectral contrast (MMD). Once the correct emissivities are found, a final temperature can be calculated with the maximum emissivity value. Additional improvements involve a refinement of ϵ_{max} in the NEM module and refining the correction for sky irradiance using the ε_{min} -MMD final emissivity and temperature values. Finally, a quality assurance (QA) data image is produced that partly depends on outputs from TES such as convergence, final ϵ_{max}, atmospheric humidity, and proximity to clouds. More detailed discussion of QA is included later in this document.

Numerical modeling studies performed by the ASTER TEWG showed that TES can recover temperatures to within 1.5 K and emissivities to within 0.015 over most scenes, assuming well calibrated, accurate radiometric measurements (Gillespie et al. 1998).

5.1 Data Inputs

Inputs to the TES algorithm are the surface radiance, $L_{s,i}$, given by equation (4) (at-sensor radiance corrected for transmittance and path radiance), and downwelling sky irradiance term, $L_{\lambda}^{\downarrow}$, which is computed from the atmospheric correction algorithm using a radiative transfer model such as MODTRAN. Both the surface radiance and sky irradiance will be output as a separate product. The surface radiance is primarily used as a diagnostic tool for monitoring changes in Earth's surface composition. Before the surface radiance is estimated using equation (4), the accuracy of the atmospheric parameters, $L_{\lambda}^{\downarrow}$, $\tau_{\lambda}(\theta)$, $L_{\lambda}^{\uparrow}(\theta)$, is improved upon using a water vapor scaling (WVS) method (Tonooka 2005) on a band-by-band basis for each

observation using an extended multi-channel/water vapor dependent (EMC/WVD) algorithm (for more details, see HyspIRI Surface Radiance ATBD).

5.2 TES Limitations

As with any retrieval algorithm, limitations exist that depend on measurement accuracy, model errors, and incomplete characterization of atmospheric effects. The largest source of inaccuracy currently for ASTER data is the residual effect of incomplete atmospheric correction. Measurement accuracy and precision contribute to less of a degree. This problem is compounded for graybodies, which have low spectral contrast and are therefore more prone to errors in "apparent" MMD, which is overestimated due to residual sensor noise and incomplete atmospheric correction. A threshold classifier was introduced by the TEWG to partly solve this problem over graybody surfaces. Instead of using the calibration curve to estimate ε_{min} from MMD, a value of ε_{min} = 0.983 was automatically assigned when the spectral contrast or MMD in emissivity was smaller than 0.03 for graybody surfaces (e.g., water, vegetation). However, this caused artificial step discontinuities in emissivity between vegetated and arid areas.

At the request of users, two parameter changes were made to the ASTER TES algorithm on August 1, 2007, first described in Gustafson et al. (2006). Firstly, the threshold classifier was removed as it caused contours and artificial boundaries in the images that users could not tolerate in their analysis. The consequence of removing the threshold classifier was a smoother appearance for all images but at the cost of TES underestimating the emissivity of graybody scenes, such as water by up to 3% and vegetation by up to 2% (Hulley et al. 2008). The second parameter change removed the iterative correction for reflected downwelling radiation, which also frequently failed due to inaccurate atmospheric corrections (Gustafson et al. 2006). Using only the first iteration resulted in improved spectral shape and performance of TES.

5.3 TES Processing Flow

Figure 7 shows the processing flow diagram for the generation of the cloud masks, land-leaving radiance, VNIR reflectances, and TES temperature and emissivity, while Figure 8 shows a more detailed processing flow of the TES algorithm itself. Each of the steps will be presented in sufficient detail in the following section, allowing users to regenerate the code. TES uses input image data of surface radiance, $L_{s,i}$, and sky irradiance, $L_{\lambda}^{\downarrow}$, to solve the TIR radiative transfer equation. The output images will consists of six emissivity images (ϵ_i) corresponding to HyspIRI bands 3–8 and one surface temperature image (T).

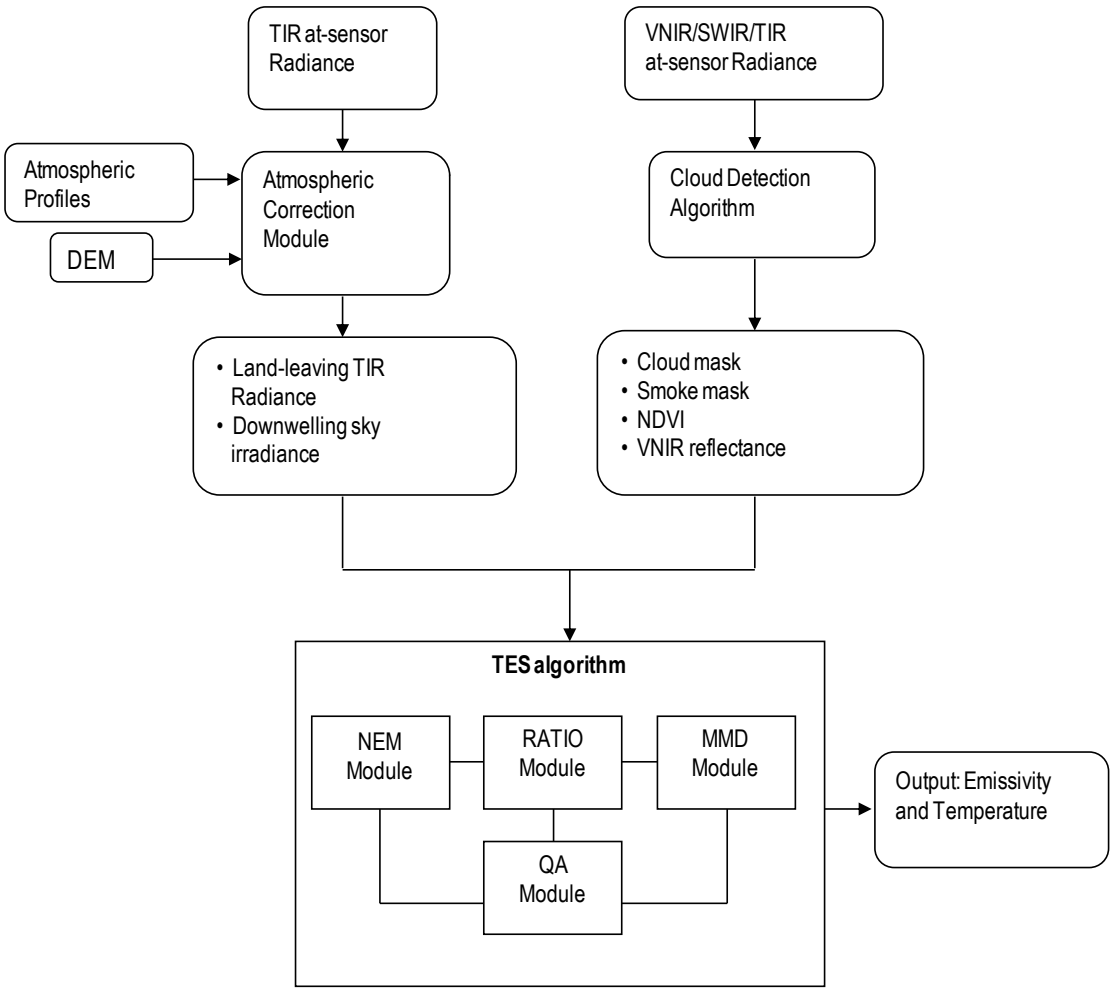

Figure 7. Flow diagram showing all steps in the retrieval process in generating the HyspIRI land surface temperature and emissivity product starting with thermal infrared (TIR) at-sensor radiances and progressing through atmospheric correction, cloud detection, and the temperature emissivity separation (TES) algorithm.

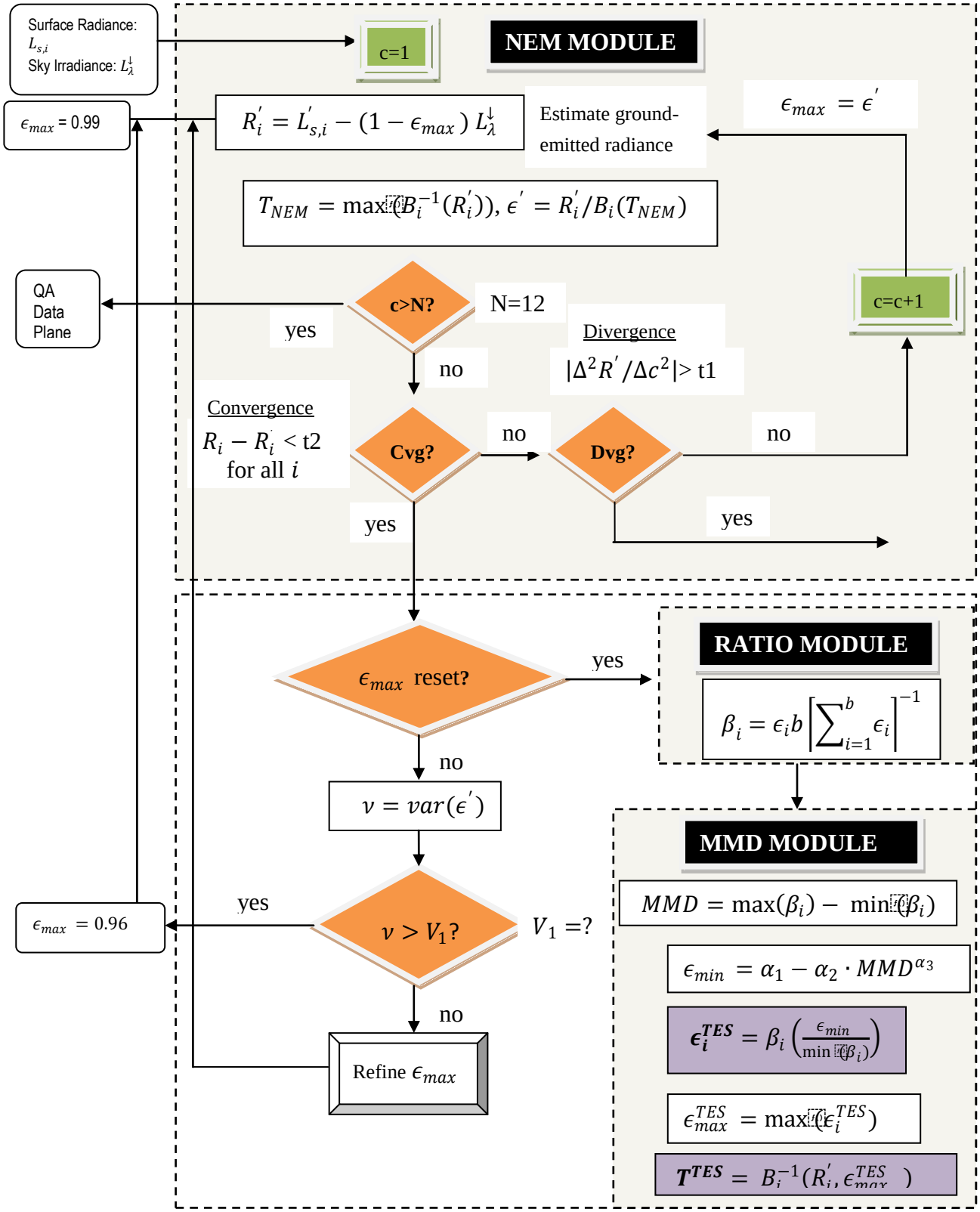

Figure 8. Flow diagram of the temperature emissivity separation (TES) algorithm in its entirety, including the NEM, RATIO and MMD modules. Details are included in the text, including information about the refinement of ϵ_{max}.

5.4 NEM Module

The normalized emissivity method (NEM) builds upon the model emissivity algorithm (Lyon 1965) by allowing the initial ϵ_{max} value to be consistent for all wavelengths. The role of NEM is to compute the surface kinetic temperature, T, and a correct shape for the emissivity spectrum. An initial value of 0.99 is set for ϵ_{max}, which is typical for most vegetated surfaces, snow, and water. For geologic materials such as rocks and sand, ϵ_{max} values are set lower than this, typically 0.96, and this value remains fixed. For all other surface types, a modification to the original NEM allows for optimization of ϵ_{max} using an empirically based process. For the majority of materials in the ASTER spectral library, a typical range for ϵ_{max} is $0.94<\epsilon_{max}<1.0$. Therefore, for a material at 300 K, the maximum errors that NEM temperatures should have are ~±1.5 K, assuming the reflected sky irradiance has been estimated correctly.

5.5 Subtracting Downwelling Sky Irradiance

Generally the effects of sky irradiance are small with typical corrections of <1 K (Gillespie et al. 1998). However, the contribution becomes larger for pixels with low emissivity (high reflectance) or in humid conditions when the sky is warmer than the surface. Over graybody surfaces (water and vegetation), the effects are small because of their low reflectivity in all bands. The first step of the NEM module is to estimate ground-emitted radiance, which is found by subtracting the reflected sky irradiance from the surface radiance term:

$$R_i = L'_{s,i} - (1 - \epsilon_{max})\, L^{\downarrow}_{\lambda} \quad (5)$$

The NEM temperature, which we call T_{NEM}, is then estimated by inverting the Planck function for each band using ϵ_{max} and the ground-emitted radiance and then taking the maximum of those temperatures. The maximum temperature will most likely be closest to the actual surface temperature in the presence of uncompensated atmospheric effects.

$$T_i = \frac{c_2}{\lambda_i}\left(ln\left(\frac{c_1 \epsilon_{max}}{\pi R_i \lambda_i^5} + 1\right)\right)^{-1} \quad (6)$$

$$T_{NEM} = \max(T_i) \quad (7)$$

The NEM emissivity spectrum is then calculated as the ratio of emitted radiance to that of a blackbody with a temperature estimated by T_{NEM}:

$$\epsilon_i^{'} = \frac{R_i}{B_i(T_{NEM})} \quad (8)$$

The new emissivity spectrum is then used to re-calculate $R_i^{'} = L_{s,i}^{'} - (1 - \epsilon_i^{'})\, L_\lambda^{\downarrow}$, and the process is repeated until convergence, which is determined if the change in R_i between steps is less than a set threshold, t_2, which is set as the radiance equivalent to NEΔT of the sensor. The process is stopped if the number of iterations exceeds a limit N, set to 12. Execution of the NEM module is also aborted if the slope of R_i versus iteration, c, increases such that $|\Delta^2 R^{'}/\Delta c^2| > t_1$, where t_1 is also set to radiance equivalent of NEΔT for the sensor (still to be determined for HyspIRI). In this case, correction is not possible, TES is aborted, and NEM values of ϵ_i and T_{NEM} are reported in the QA data plane, along with an error flag. TES is also aborted and an error flag recorded if, for any iteration, the values of ϵ_i fall out of reasonable limits, set to $0.5 < \epsilon_i < 1.0$. See Figure 8 for a detailed description of these steps.

5.6 Refinement of ϵ_{max}

Most pixels at HyspIRI resolution (60 m) will contain a mixed cover type consisting of vegetation and soil, rock and water. The effective maximum emissivity for such pixels will therefore vary across the scene and depend on the fractional contribution of each cover type. For these cases, the initial ϵ_{max} = 0.99 may be set to high and refinement of ϵ_{max} is necessary to

improve accuracy of T_{NEM}. The optimal value for ϵ_{max} minimizes the variance, ν, of the NEM calculated emissivities, ϵ_i. The optimization of ϵ_{max} is only useful for pixels with low emissivity contrast (near graybody surfaces) and therefore is only executed if the variance for ϵ_{max} = 0.99 is less than an empirically determined threshold (e.g., $V_1 = 1.7 \times 10^{-4}$ for ASTER) (Gillespie et al. 1998). If the variance is greater than V_1, then the pixel is assumed to predominately consist of either rock or soil. For this case, ϵ_{max} is reset to 0.96, which is a good first guess for most rocks and soils in the ASTER spectral library, which typically fall between the 0.94 and 0.99 range. If the first condition is met, and the pixel is a near-graybody, then values for ϵ_{max} of 0.92, 0.95, 0.97, and 0.99 are used to compute the variance for each corresponding NEM emissivity spectrum. A plot of variance ν versus each ϵ_{max} value results in an upward-facing parabola with the optimal ϵ_{max} value determined by the minimum of the parabola curve in the range $0.9 < \epsilon_{max} < 1.0$. This minimum is set to a new ϵ_{max} value, and the NEM module is executed again to compute a new T_{NEM}. Further tests are used to see if a reliable solution can be found for the refined ϵ_{max}. If the parabola is too flat, or too steep, then refinement is aborted and the original ϵ_{max} value is used. The steepness condition is met if the first derivative (slope of ν vs. ϵ_{max}) is greater than a set threshold (e.g., $V_2 = 1.0 \times 10^{-3}$ for ASTER) and the flatness conditions is met if the second derivative is less than a set threshold (e.g., $V_3 = 1.0 \times 10^{-3}$ for ASTER). Finally, if the minimum ϵ_{max} corresponds to a very low ν, then the spectrum is essentially flat (graybody) and the original ϵ_{max} = 0.99 is used. This condition is met if $\nu_{min} < V_4$ (e.g. $V_2 = 1.0 \times 10^{-4}$ for ASTER). These thresholds will need to be refined for the HyspIRI bands and determined empirically. Table 2 shows typical output from various stages of the TES algorithm for pixels representing three different surface types: sand dunes, vegetated cropland, and semi-vegetated cropland for an ASTER scene on July 15, 2000, over the Imperial Valley, southeastern

California. Note the different ϵ_{max} value for each of these surface types. The dune pixel was set to 0.96 due to large variance in emissivity; the fully vegetated pixel was set to 0.983, a typical value for a graybody; and ϵ_{max} for the semi-vegetated pixel needed to be optimized, resulting in a final value of 0.969.

Table 2. Output from various stages of the TES algorithm for three surface types; sand dunes, vegetated cropland, and semi-vegetated cropland for an ASTER scene on July 15, 2000, over the Imperial Valley, southeastern California.

	Algodones Dunes	Cropland (vegetated)	Cropland (semi-vegetated)
ϵ_{max}	0.96	0.983	0.969
MMD	0.189	0.013	0.028
ϵ_{min}	0.793	0.967	0.944
T_{NEM}	337.06 K	305.92 K	319.75 K
T_{TES}	337.41 K	306.14 K	319.65 K

5.7 Ratio Module

In the ratio module, the NEM emissivities are ratioed to their average value to calculate a β_i spectrum as follows:

$$\beta_i = \frac{\epsilon_i}{\bar{\epsilon}} \tag{9}$$

Typical ranges for the β_i emissivities are $0.75 < \beta_i < 1.32$, given that typical emissivities range from 0.7 to 1.0. Errors in the β_i spectrum due to incorrect NEM temperatures are generally systematic.

5.8 MMD Module

In the minimum-maximum difference (MMD) module, the β_i emissivities are scaled to an actual emissivity spectrum using information from the spectral contrast or MMD of the β_i spectrum. The MMD can then be related to the minimum emissivity, ϵ_{min}, in the spectrum using an empirical relationship determined from lab measurements of a variety of different spectra,

including rocks, soils, vegetation, water, and snow/ice. From ϵ_{min} , the actual emissivity spectrum can be found by re-scaling the β_i spectrum. First, the MMD of the β_i spectrum is found by:

$$MMD = \max(\beta_i) - \min(\beta_i) \quad (10)$$

Then MMD can be related to ϵ_{min} using a power-law relationship:

$$\epsilon_{min} = \alpha_1 - \alpha_2 MMD^{\alpha_3}, \quad (11)$$

where α_j are coefficients that are obtained by regression using lab measurements. For the six nominal HyspIRI TIR bands between 8 and 12 µm (shown in Figure 1), the values for the coefficients were calculated as α_1= 0.997, $\alpha_2 = 0.7050$, and $\alpha_3 = 0.7430$. The TES emissivities are then calculated by re-scaling the β_i emissivities:

$$\epsilon_i^{TES} = \beta_i \left(\frac{\epsilon_{min}}{\min(\beta_i)} \right) \quad (12)$$

An example TES emissivity output image for ASTER band 12 (9.1 µm) is shown in Figure 9 (a) for an ASTER scene acquired on July 15, 2000, over the Imperial Valley, southeastern California. Bare areas, such as the Algodones Dunes running diagonally across the southeast corner, generally have emissivity <0.85, while graybody surfaces such as the Imperial Valley croplands and Salton Sea in the southwest corner of the image have higher emissivities >0.95. Figure 10 shows the differences in emissivity spectra between the NEM and TES output for pixels over three different surface types (sand dunes, vegetated cropland, and semi-vegetated cropland) for the ASTER Imperial Valley scene. Note that, although both NEM and TES have similar spectral shape, the emissivities of NEM are lower than TES because of errors in the initial estimate of ϵ_{max} in the NEM module. The Algodones Dunes spectrum has high spectral contrast that is typical for a quartz spectrum that has the characteristic quartz doublet in the 8–10-µm region, while the emissivity of vegetation is usually spectrally flat, and high.

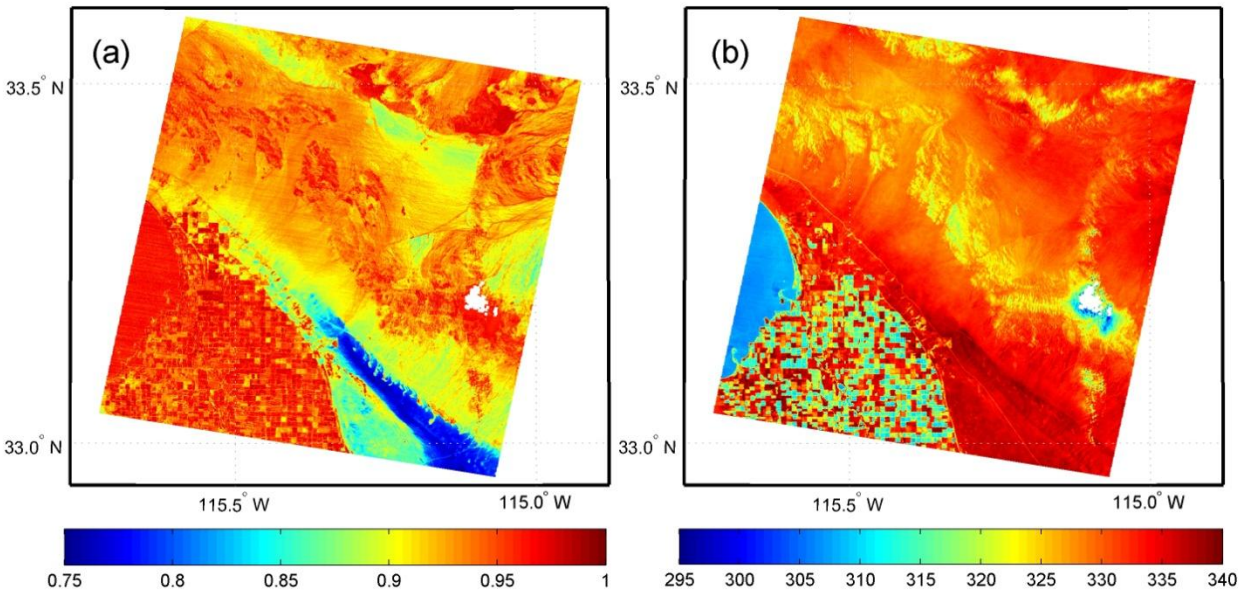

Figure 9. (a) ASTER land surface emissivity for band 12 (9.1 µm) and (b) surface temperature products output from the TES algorithm over the Imperial Valley, southeastern California on July 15, 2000.

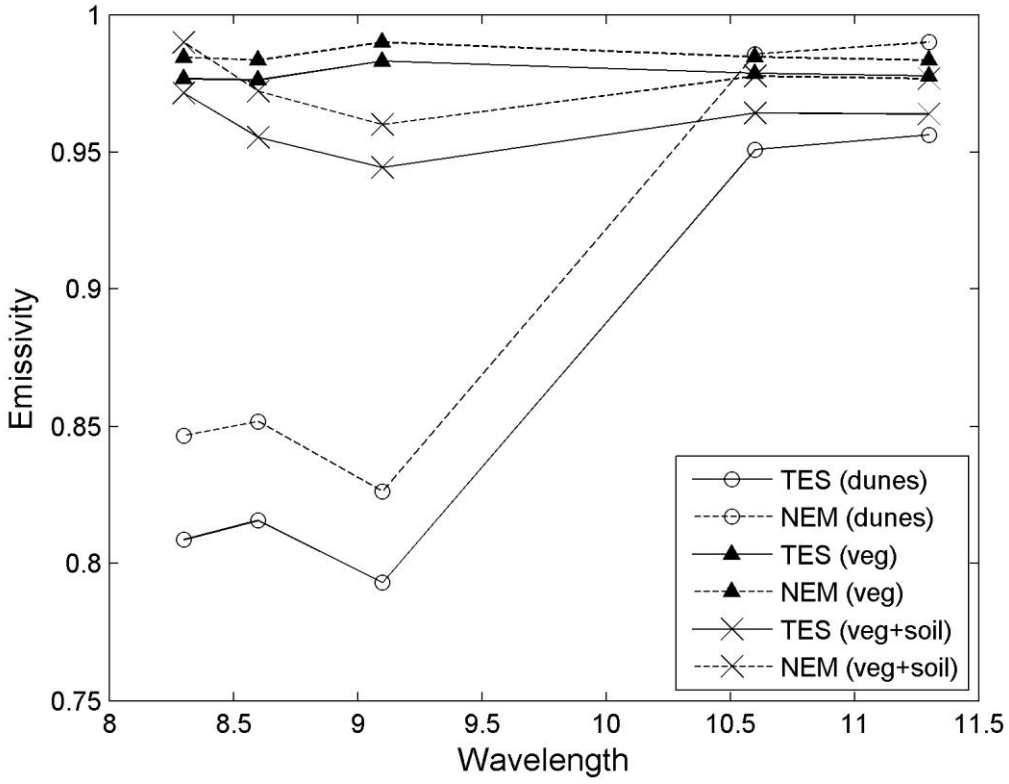

Figure 10. ASTER derived TES and NEM emissivity spectra for three different surfaces in the ASTER scene shown in Figure 9: Algodones Dunes, full vegetation crops, and partially vegetated crops with a soil component. Details of the TES and NEM outputs from these spectra are shown in Table 2.

For pixels with low spectral contrast (e.g., graybody surfaces), the accuracy of MMD calculated from TES is compromised and approaches a value that depends on measurement error and residual errors from incomplete atmospheric correction. For ASTER, which has a NEΔT of 0.3 K at 300 K, measurement error contributes to the apparent contrast, and a method was explored to correct the apparent MMD using Monte Carlo simulations. For HyspIRI (NEΔT of 0.05 K), we expect measurement errors to be minimal and atmospheric effects to be the largest contribution to MMD errors. A further problem for graybody surfaces is a loss of precision for low MMD values. This is due to the shape of the power-law curve of ϵ_{min} vs. MMD at low MMD values, where small changes in MMD can lead to large changes in ϵ_{min}. To address these issues, the ASTER TEWG initially proposed a threshold classifier for graybody surfaces. If MMD<0.03, the value of ϵ_{min} in equation (12) was set to 0.983, a value typical for water and most vegetated surfaces. However, this classification was later abandoned as it introduced large step discontinuities in most images (e.g., from vegetation to mixed-cover types).

The consequence of removing the threshold classifier was that over graybody surfaces errors in emissivity could range from 0.01 to 0.05 (0.5 K to 3 K) due to measurement error and residuals errors from atmospheric correction (Gustafson et al. 2006; Hulley and Hook 2009b).

For HyspIRI, we expect to use original TES without classification and use the WVS method to correct the atmospheric parameters on a pixel-by-pixel basis. This method is described in the Surface Radiance ATBD and was not fully developed when the ASTER algorithm was developed.

For bare surfaces (rocks, soils, and sand), the error in NEM calculated T may be as much as 2–3 K, assuming a surface at 340 K due to the fixed assumption of ϵ_{max} = 0.96. This error can be corrected by recalculating T using the TES retrieved maximum emissivity, ϵ_{max}^{TES}, and the

atmospherically corrected radiances, R_i. The maximum emissivity used as correction for reflected $L_\lambda^\downarrow$ will be minimal.

$$T^{TES} = \frac{c_2}{\lambda_{max}} \left(ln \left(\frac{c_1 \epsilon_{max}^{TES}}{\pi R_i \lambda_{max}^5} + 1 \right) \right)^{-1} \quad (13)$$

An example TES surface temperature output image is shown in Figure 9 (b) for the ASTER Imperial Valley scene. Bare areas, such as the Algodones Dunes running diagonally across the southeast corner, generally have the highest temperatures with T>335 K, while graybody surfaces such as the Imperial Valley croplands and Salton Sea in the southwest corner have the coolest temperatures with T<315 K.

In the original ASTER algorithm, a final correction is made for sky irradiance using the TES temperature and emissivities; however, this was later removed, as correction was minimal and influenced by atmospheric correction errors. This additional correction will not be used for HyspIRI.

5.9 MMD vs. ϵ_{min} Regression

The relationship between MMD and ϵ_{min} is physically reasonable and is determined using a set of laboratory spectra in the ASTER spectral library v2.0 (Baldridge et al. 2009) and referred to as the calibration curve. The original ASTER regression coefficients were determined from a set of 86 laboratory reflectance spectra of rocks, soils, water, vegetation, and snow supplied by J.W. Salisbury from Johns Hopkins University. One question that needed to be answered was whether using a smaller or larger subset of this original set of spectra changed the results in any manner. Establishing a reliable MMD vs. ϵ_{min} relationship with a subset of spectral representing all types of surfaces is a critical assumption for the calibration curve. This assumption was tested using various combinations and numbers of different spectra (e.g.,

Australian rocks, airborne data, and a subset of 31 spectra from Salisbury), and all yielded very similar results to the original 86 spectra.

For HyspIRI, the original 86 spectra were updated to include additional sand spectra used to validate the North American ASTER Land Surface Emissivity Database (NAALSED) (Hulley and Hook 2009b) and additional spectra for vegetation from the MODIS spectral library and ASTER spectral library v2.0, giving a total of 150 spectra. The data were convolved to the nominal HyspIRI bands and ϵ_{min} and β_i spectra calculated using equation (9) for each sample. The MMD for each spectra was then calculated from the β_i spectra and regressed to the ϵ_{min} values. The relationship follows a simple power law given by equation (11), with regression coefficients $\alpha_1 = 0.997$, $\alpha_2 = 0.7050$, and $\alpha_3 = 0.7430$, and $R^2 = 0.987$. Figure 11 shows the power-law relationship between MMD and ϵ_{min} using the 150 lab spectra.

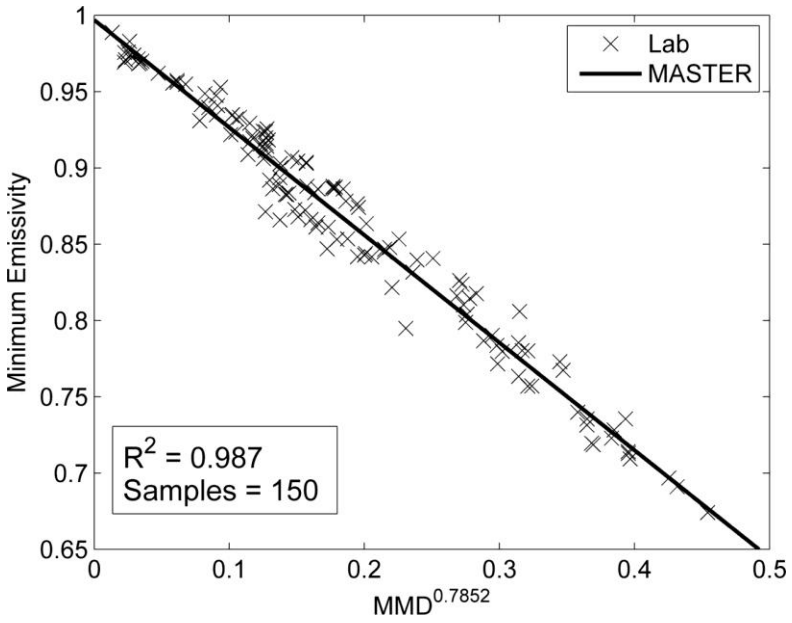

Figure 11. HyspIRI calibration curve of minimum emissivity vs. min-max difference (MMD). The lab data (crosses) are computed from 150 spectra consisting of a broad range of terrestrial materials (rocks, sand, soil, water, vegetation, and ice).

5.10 Atmospheric Effects

The accuracy of the atmospheric correction technique used to estimate the surface radiance relies on the accuracy of the variables input to the radiative transfer model (e.g., air temperature, relative humidity, and ozone). A sensitivity analysis (see Surface Radiance ATBD) showed that a change in atmospheric water vapor of 10% leads to a 2.1% change in radiance for the nominal HyspIRI band 3 (8.3 μm), which is the most susceptible to atmospheric absorption and emission of all bands, while a change in air temperature of 1 K leads to a -1.3% change in radiance, both for a standard tropical atmospheric profile. Changes in ozone and aerosol amount have much smaller effects, although for ASTER band 5 (9.1 μm), which is closer to the ozone absorption region, doubling the ozone resulted in a 2.2% change in radiance. These atmospheric errors tend to be highly correlated from band to band, since each channel has a characteristic absorbing feature. As a result, the effect on TES output is usually relatively small, but if these errors are uncorrelated from band to band then much larger errors can occur, particularly for graybodies, where small changes in MMD can significantly alter the shape of the emissivity spectrum. For example, over water bodies, errors in emissivity of up to 3% (0.03) have been found due to uncompensated atmospheric effects (Hulley and Hook 2009b; Tonooka and Palluconi 2005).

One method for improving the accuracy of the surface radiance product is to apply the WVS method (Tonooka 2005). Using 183 ASTER scenes over lakes, rivers, and sea surfaces, it was found that using the WVS method instead of the standard atmospheric correction improved estimates of surface temperature from 3 to 8 K in regions of high humidity (Tonooka 2005). These are substantial errors when considering the required accuracy of the TES algorithm is

~1 K (Gillespie et al. 1998). The WVS method is described in more detail in the HyspIRI Surface Radiance ATBD.

Figure 12 shows emissivity spectra over the Salton Sea, showing the effects of applying the WVS atmospheric correction method on the shape of the emissivity spectrum when compared to using the standard (STD) correction method without WVS. The emissivity spectrum of water is high (~0.98) and flat and the results in Figure 12 show a dramatic improvement in emissivity accuracy in both magnitude (up to 0.06 for ASTER band 11, and 0.09 for MODIS band 29) and spectral shape when using the WVS as opposed to the STD method. Because of the humid day, where MOD07 PWV values were around 4 cm over the water, the spectral contrast of the STD emissivity results are overestimated for ASTER and MODIS data. However, when applying the WVS method, the ASTER emissivity spectra fall within 0.015 of the lab-measured spectrum, while MODIS emissivity spectra are within 0.005 at all wavelengths. Differences between the 3-and 5-band TES algorithm applied to ASTER data were small.

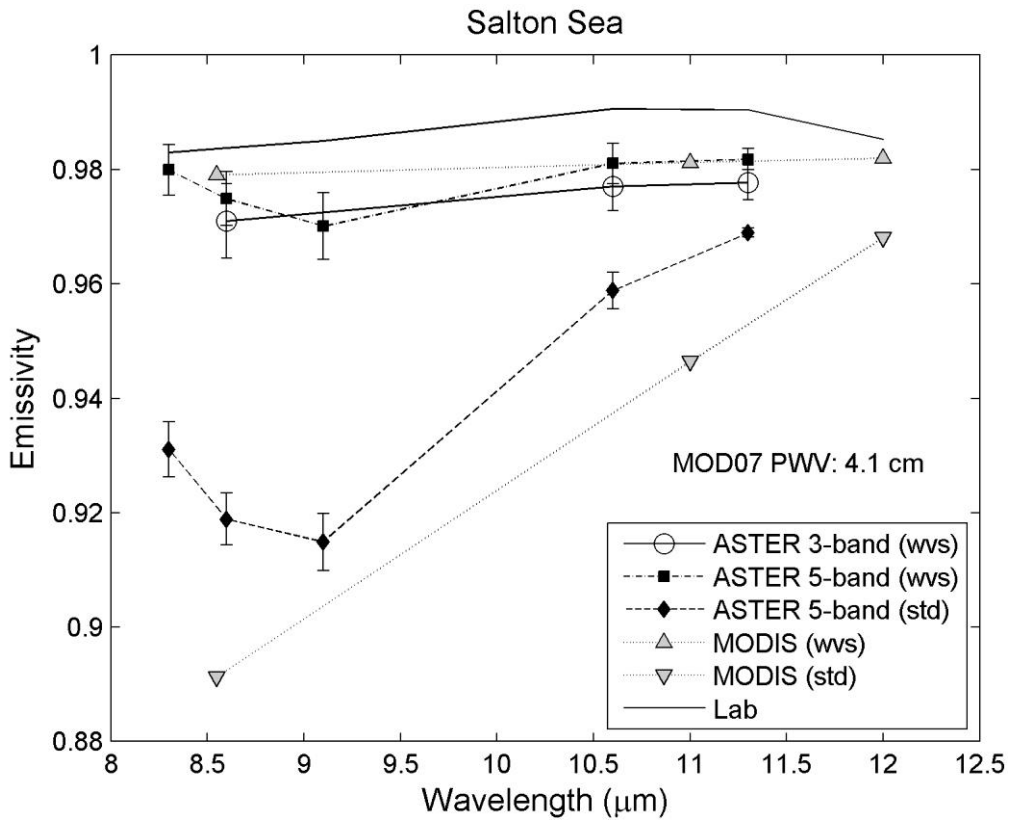

Figure 12. Emissivity spectra comparisons for the Salton Sea on June 15, 2000, between ASTER (3-band), ASTER (5-band), and MODIS, using the TES algorithm along with lab spectra of water from the ASTER spectral library. Results from the water vapor scaling (WVS) method and the standard (STD) atmospheric correction are also shown. An estimate of the precipitable water vapor (PWV) from the MOD07 atmospheric product indicates very high humidity on this day.

6 Quality Assessment and Diagnostics

The T and ϵ products will need to be assessed using a set of quality control (QC) flags. These QC flags will involve automatic tests processed internally for each pixel and will depend on various retrieval conditions such as whether the pixel is over land or ocean surface, the atmospheric water vapor content (dry, moist, very humid, etc.), and cloud cover. The data quality attributes will be set automatically according to parameters set on data conditions during algorithm processing and will be assigned as either "bad," "suspect," or "good." Estimates of the accuracy and precision of the T and ϵ product will be reported in a separate data plane. At each step in the TES algorithm, various performance information will be output, which will give the

user a summary of algorithm statistics in a spatial context. This type of information will be useful for determining surface type, atmospheric conditions, and overall performance of TES.

The architecture of the HyspIRI T and ϵ QA data plane will closely resemble that of ASTER (Gillespie et al. 1998). It will consist of header information followed by three 8-bit QA data planes. The structure of the first QA data plane will consist of three primary fields, which are detailed in Table 3:

1. Data Quality Field: "bad," "suspect," or "good" to be assigned to specific bit patterns.
2. Cloud Mask Field: Outputs from cloud mask statistics, e.g., optically thick or thin cloud, cirrus or contrails, clear, or snow/ice determined from NDSI threshold.
3. Cloud Adjacency: Clear pixels defined in the cloud mask will be assigned an adjacency category dependent on distance to the nearest cloud defined quantitatively by the number of pixels (e.g., very close, close, far, very far).

The structure of the second QA data plane will consist of performance metrics output from various stages of the TES algorithm, detailed in Table 4:

1. The final value of ϵ_{max} used in the NEM module after optimization (if necessary).
2. Number of iterations needed to remove reflected downwelling sky irradiance.
3. Atmospheric opacity test for humid scenes, using $L_\lambda^\downarrow / L^{'}$ test.
4. MMD regime: MMD<0.3 (near-graybody) or MMD>0.3 (likely bare).

Table 3. Quality assurance (QA) data plane 1 description of the three data fields: data quality, cloud mask, and cloud adjacency.

Data Field	Category	Bits	Description
Data Quality	"Excellent"	11	Good quality, no further QA info necessary
	"Good"	10	Good quality, but possible cloud adjacency effects; further QA examination necessary.
	"Suspect"	01	Out of range data values Suspect input quality data flag Perimeter effects from thick/thin cloud Humid scene Fairly calibrated
	"Bad"	00	Bad pixel labeled in L1A data TES algorithm abort flag TES algorithm divergence flag TES convergence issues (only NEM values output) Poorly calibrated, or ocean pixel
Cloud Mask	Thick cloud	11	Optically thick cloud detected with high reflectance
	Thin cloud	10	Optically thin cloud detected with medium or low reflectance
	Cirrus	01	Cirrus test indicated cirrus, haze, or jet contrails present
	Clear	00	No clouds detected
Cloud Adjacency	Very near	11	Pixel is <5 pixels from nearest cloud
	Near	10	Pixel within 5–15 pixels of nearest cloud
	Far	01	Pixel within 15–30 pixels of nearest cloud
	Very far	00	Pixel >30 pixels from nearest cloud

Table 4. Quality assurance (QA) data plane 2 description of output diagnostics from the TES algorithm.

Data Field	Category	Bits	Description
ϵ_{max}	>0.98	11	Graybodies (water, vegetation, snow)
	0.96-0.98	10	Nominal value
	0.94-0.96	01	Bare surfaces, silicate rocks
	<0.94	00	Error condition (atmospheric correction)
Iterations	≥7	11	Slow convergence
	6	10	Nominal performance
	5	01	Nominal performance
	4	00	Fast convergence
$L_\lambda^\downarrow / L^{'}$	≥0.3	11	Warm, humid air; or cold land
	0.2-0.3	10	Nominal value
	0.1-0.2	01	Nominal value
	≥0.1	00	Dry conditions, or high altitude scene
MMD	≥0.3	10	Low spectral contrast, graybody surface
	>0.3	00	High spectral contrast, most bare surfaces

7 Numerical Simulations

Numerical simulations will be run on the TES algorithm to analyze performance for a wide range of different conditions and surfaces. It has been shown that when TES operates on true radiances (error free), temperatures can be recovered to within 1 K and emissivities to 0.01 for a wide range of surfaces. The performance was related to scatter about the ϵ_{min} - MMD curve, and not to composition of the material.

The following simulations will be run using the nominal HyspIRI bands to assess the performance of TES:

1. Sensitivity of TES results to T and ϵ_{max} from the NEM module for a range of temperatures from 240 to 340 K.

2. Error dependence of NEM temperatures on initial value selected for ϵ_{max}. This will be accomplished by varying ϵ_{max} over a wide range (0.94–1) in the NEM module to estimate the range in temperatures calculated from NEM.
3. Error dependence of NEM ϵ spectrum with regard to tilt and amplitude for selected values of ϵ_{max}.
4. Sensitivity of NEM and TES outputs to NEΔT. It has been shown that TES is not as sensitive to NEΔT as NEM for ASTER data, but this has to be shown with HyspIRI bands.
5. It has been shown that TES's performance can be improved by using the final TES temperature to recalculate the ratio emissivities and the TES emissivities from the calibration curve. Improvements of around 0.01 in emissivity were found but depend on the sample being retrieved. Tests need to be run with HyspIRI-like datasets to assess whether this extra computing time would be worthwhile for improved accuracy.
6. A comprehensive sensitivity analysis is required to quantify how uncertainties in atmospheric parameters relate to TES accuracy. Atmospheric correction errors will be minimized by using the WVS method, but variations in the atmospheric parameters from band to band will still produce significant error in TES emissivity spectral shape and amplitude.

8 Validation Strategies

8.1 Pre-launch

It is expected that a beta version of the HyspIRI atmospheric correction production algorithm will be ready at least two years prior to launch, depending on the choice of atmospheric profile data, and made available at the Land Processes DAAC (LP DAAC). A simulation test dataset will be used to verify that the algorithm runs correctly at the LPDAAC, and subsequent changes and improvements to the beta version will be uploaded prior to launch.

The bulk of the atmospheric correction validation will involve testing and validation with JPL's Hyperspectral Thermal Emission Spectrometer (HyTES), an airborne sensor that has been developed specifically for support of the HyspIRI mission. The higher spatial (~3-30 m) and spectral resolution (256 bands from 7.5 to 12 μm) will help determine the optimal band placements for the HyspIRI bands and assist with algorithm development. The first HyTES flights are scheduled for late 2012.

8.2 Post-launch

While the land surface temperature products from the ASTER TES algorithm have been validated by several authors (Coll et al. 2005; Hook et al. 2007; Tonooka and Palluconi 2005), far fewer authors have attempted to validate the surface emissivity product (Schmugge and Ogawa 2006; Schmugge et al. 2003). Currently, the most comprehensive emissivity validation of the ASTER product was performed in validating the North American ASTER Land Surface Database (NAALSED) v2.0 emissivity product (Hulley et al. 2009a). NAALSED was validated over arid/semi-arid regions using nine pseudo-invariant sand dune sites in the western/southwestern USA. The emissivity of samples collected at each of the nine sites was determined in the laboratory using a Nicolet 520 FT-IR spectrometer and convolved with the

appropriate ASTER system response functions. Validation of emissivity data from space ideally requires a site that is homogeneous in emissivity at the scale of the imagery, allowing several image pixels to be validated over the target site. HyspIRI will meet this requirement due to its high spatial resolution of 60 m, making it unique amongst other spaceborne sensors that provide emissivity products at much coarser spatial resolutions, such as MODIS at 1 km. The nine sand dune validation sites chosen for the ASTER study and planned for use with HysPIRI are: Great Sands National Park, Colorado; White Sands National Monument, New Mexico; Kelso Dunes, California; Algodones Dunes, California; Stovepipe Wells Dunes, California; Coral Pink Sand Dunes, Utah; Little Sahara Dunes, Utah; Killpecker Dunes, Wyoming; and Moses Lake Basalt Dunes, Washington.

For HyspIRI we plan to use in-situ data from a variety of ground sites covering the majority of different land cover types defined in the International Geosphere-Biosphere Programme (IGBP). The sites will consist of water, vegetation (forest, grassland, and crops), and barren areas (Table 5).

Table 5: The core set of global validation sites according to IGBP class to be used for validation and calibration of the HyspIRI sensor.

IGBP Class		Sites
0	Water	Tahoe, Salton Sea, CA
1,2	Needle-leaf forest	Krasnoyarsk, Russia; Tharandt, Germany; Fairhope, Alaska
3,4,5	Broad-leaf/mixed forest	Chang Baisan, China; Hainich, Germany; Hilo, Hawaii
6,7	Open/closed shrublands	Desert Rock, NV; Stovepipe Wells, CA
8,9,10	Savannas/Grasslands	Boulder, CO; Fort Peck, MT
12	Croplands	Bondville, IL; Penn State, PA; Sioux Falls, SD; Goodwin Creek, MS
16	Barren	Algodones dunes, CA; Great Sands, CO; White Sands, NM; Kelso Dunes, CA; Namib Desert, Namibia; Kalahari Desert, Botswana

8.2.1 Water Targets

For water surfaces, we will use the Lake Tahoe, California/Nevada automated validation site where measurements of skin temperature have been made every two minutes since 1999 and are used to validate the mid and thermal infrared data and products from ASTER and MODIS (Hook et al. 2007). Water targets are ideal for calval activities because they are thermally homogeneous and the emissivity is generally well known. A further advantage of Tahoe is that the lake is located at high altitude, which minimizes atmospheric correction errors, and is large enough to validate sensors from pixel ranges of tens of meters to several kilometers. The typical range of temperatures at Tahoe is from 5°C to 25°C. More recently in 2008, an additional calval site at the Salton Sea was established. Salton Sea is a low-altitude site with significantly warmer temperatures than Lake Tahoe (up to 35°C), and together they provide a wide range of different conditions.

8.2.2 Vegetated Targets

For vegetated surfaces (forest, grassland, savanna, and crops), we will use a combination of data from the Surface Radiation Budget Network (SURFRAD), FLUXNET, and NOAA-CRN sites. For SURFRAD, we will use a set of six sites established in 1993 for the continuous, long-term measurements of the surface radiation budget over the United States through the support of NOAA's Office of Global Programs (http://www.srrb.noaa.gov/surfrad/). The six sites (Bondville, IL; Boulder, CO; Fort Peck, MT; Goodwin Creek, MS; Penn State, PA; and Sioux Falls, SD) are situated in large, flat agricultural areas consisting of crops and grasslands and have previously been used to assess the MODIS and ASTER LST&E products with some success (Wang and Liang, 2009; Augustine et al. 2000). From FLUXNET and the Carbon Europe Integrated Project (http://www.carboeurope.org/), we will include an additional four sites to

cover the broadleaf and needleleaf forest biomes (e.g., Hainich and Tharandt in Germany; Chang Baisan, China; Krasnoyarsk, Russia), using data from the FLUXNET as well as data from the EOS Land Validation Core sites (http://landval.gsfc.nasa.gov/coresite_gen.html). Furthermore, the U.S. Climate Reference Network (USCRN) has been established to monitor present and future long-term climate data records (http://www.ncdc.noaa.gov/crn/). The network consists of 114 stations in the continental USA and is monitored by NOAA's National Climatic Data Center (NCDC). Initially, we plan to use the Fairhope, Alaska, and Hilo, Hawaii, sites from this network.

8.2.3 Barren Targets

For LST validation over arid regions, we will use a set of nine pseudo-invariant, homogeneous sand dune sites in the southwestern USA (Hulley et al. 2009a) which were used for validating ASTER and MODIS products and two sites over large sand dune seas in the Namib and Kalahari deserts in Southern Africa (Hulley et al. 2009b) for validating AIRS. The emissivity and mineralogy of samples collected at these sites have been well characterized and are described by Hulley et al. (2009a).

8.2.3.1 Sand Dune Validation Targets

Pseudo-invariant ground sites such as playas, salt flats, and claypans have been increasingly recognized as optimal targets for the long-term validation and calibration of visible, shortwave, and thermal infrared data (Bannari et al. 2005; Cosnefroy et al. 1996; de Vries et al. 2007). We have found that large sand dune fields are particularly useful for the validation of TIR emissivity data (Hulley and Hook 2009a). Sand dunes have consistent and homogeneous mineralogy and physical properties over long time periods. They do not collect water for long periods as playas and pans might, and drying of the surface does not lead to cracks and fissures,

typical in any site with a large clay component, which could raise the emissivity due to cavity radiation effects (Mushkin and Gillespie 2005). Furthermore, the mineralogy and composition of sand samples collected in the field can be accurately determined in the laboratory using reflectance and x-ray diffraction (XRD) measurements. In general, the dune sites should be spatially uniform and any temporal variability due to changes in soil moisture and vegetation cover should be minimal. Ideally, the surface should always be dry, since any water on the surface can increase the emissivity by up to 0.16 (16%) in the 8.2–9.2-μm range depending on the type of soil (Mira et al. 2007).

Figure 13 shows ASTER false-color visible images of each dune site and comparisons between the emissivity spectra from NAALSED and the lab measurements. The lab spectra in Figure 13 show the mean and standard deviation (spatial) in emissivity for all sand samples collected at the site, while the NAALSED spectra give the mean emissivity and combined spatial and temporal standard deviation for all observations acquired during the winter (Jan.–Mar.) and summer (July–Sept.) time periods. The results show that TES-derived emissivity from ASTER data captures the spectral shape of all the dune sands very well. The quartz doublet centered around ASTER band 11 (8.6 μm) is clearly visible for Algodones Dunes samples, and the characteristic gypsum minimum in ASTER band 11 (8.6 μm) is evident from the White Sands samples.

Seasonal changes in vegetation cover, aeolian processes such as wind erosion, deposition and transport, and daily variations in surface soil moisture from precipitation, dew, and snowmelt are the primary factors that could potentially affect the temporal stability and spatial uniformity of the dune sites. Field observations during the spring and early summer of 2008 revealed that the major portion of the dune sites was bare, with the exception of Kelso and Little Sahara,

which contained sparse desert grasses and reeds on the outer perimeter of the dune field and in some interdunal areas. Nonetheless, this does not mean the other seven dune sites did not have vegetation in the past, since 2000. The presence of soil moisture would result in a significant increase in TIR emissivity at the dune sites, caused by the water film on the sand particles decreasing its reflectivity (Mira et al. 2007; Ogawa et al. 2006), particularly for HyspIRI bands 3–5 in the quartz Reststrahlen band. However, given that the majority of dune validation sites are aeolian (high winds), at high altitude (low humidity), and in semi-arid regions (high skin temperatures), the lifetime of soil moisture in the first few micrometers of the surface skin layer as measured in the TIR is most likely small due to large sensible heat fluxes and, therefore, high evaporation rates, in addition to rapid infiltration. Consequently, we hypothesize that it would most likely take a very recent precipitation event to have any noticeable effect on remote-sensing observations of TIR emissivity over these types of areas.

For LST validation over the sand dune sites, we will use a recently established radiance-based (R-based) validation method (Coll et al. 2009; Wan and Li 2008). The advantage of this method is that it does not require in-situ measurements, but instead relies on atmospheric profiles of temperature and water vapor over the site and an accurate estimation of the emissivity. The method involves using a radiative transfer model such as MODTRAN (Berk et al. 2005) with the input profiles and surface emissivity to compute two TOA radiance values corresponding to two LST values close to the retrieved LST value in an atmospheric window region (e.g., 11 μm). The theoretically correct LST is then estimated by linear interpolation between the two TOA radiance values and the retrieved LST value. The advantage of the R-based method is that it can be applied to a large number of global sites where the emissivity is known (e.g. from field

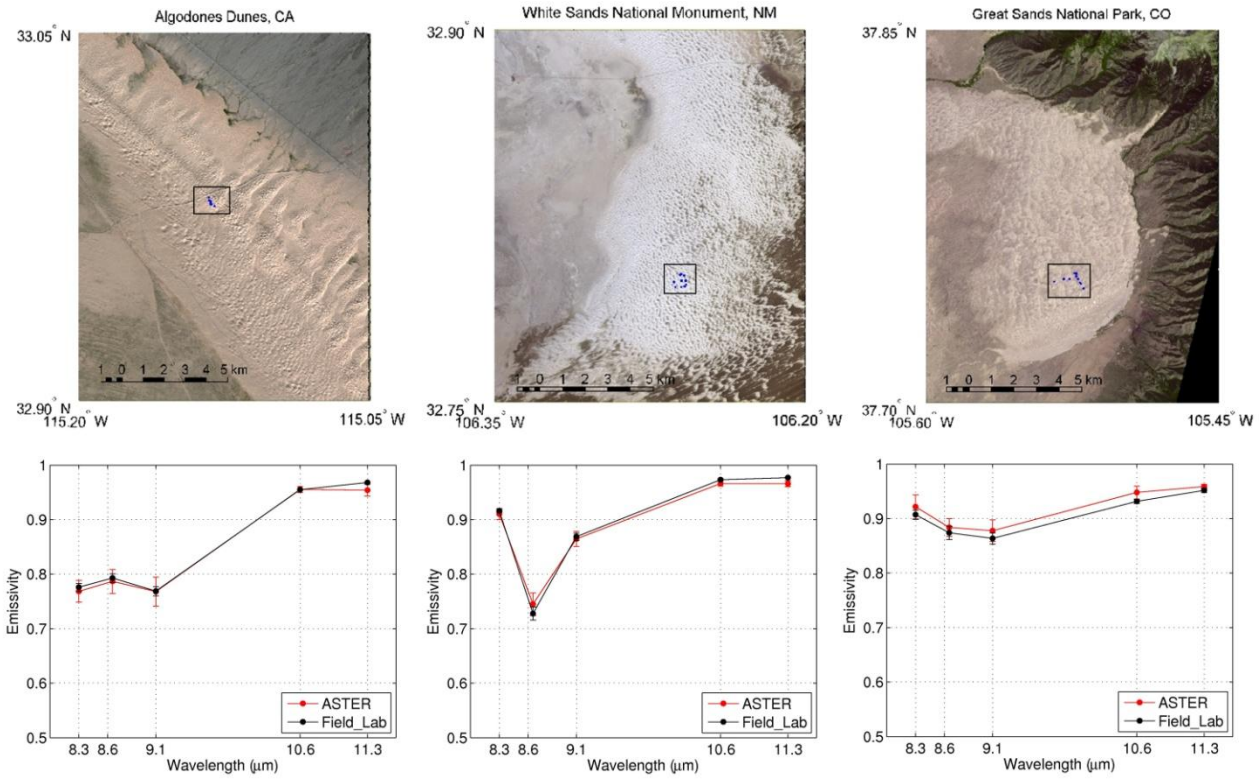

Figure 13. ASTER false-color visible images (top) and emissivity spectra comparisons between ASTER TES and lab results for Algodones Dunes, California; White Sands, New Mexico; and Great Sands, Colorado (bottom). Squares with blue dots indicate the sampling areas. ASTER error bars show temporal and spatial variation, whereas lab spectra show spatial variation.

measurements) and during night- and daytime observations to define the diurnal temperature range. Figure 14 shows an example of the R-based method applied to Atmospheric Infrared Sounder (AIRS) LST data over the Namib Desert using observations from 2003 to 2009. Emissivity data from lab measurements of sand samples collected from the Namib Desert and NCEP atmospheric profile data were used for input to the AIRS SARTA radiative transfer model.

Figure 15 shows emissivity spectra from sand dune samples collected at various sites in the southwestern USA. The spectra cover a wide range of emissivities in the TIR region. These

sites will be used to validate HyspIRI emissivity and temperature products using the R-based method.

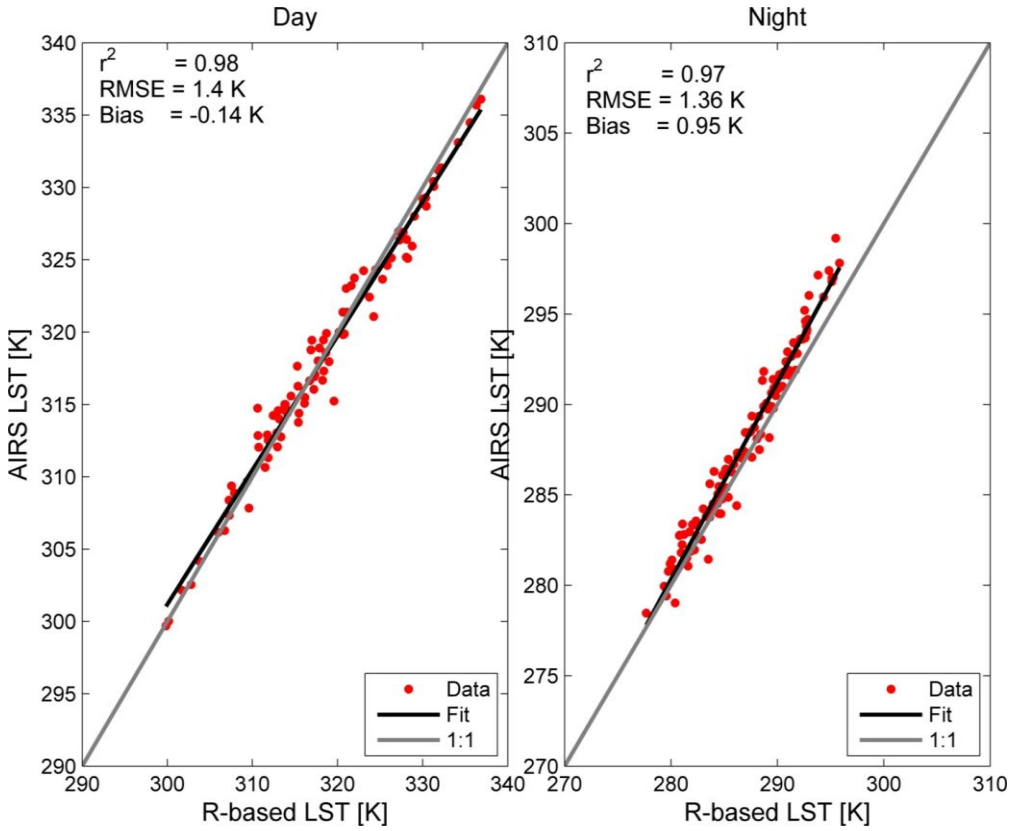

Figure 14. An example of the Radiance-based method applied to Atmospheric Infrared Sounder (AIRS) LST data over the Namib Desert using observations from 2003 to 2009. Emissivity data from lab measurements of sand samples collected from the Namib Desert and atmospheric profiles from NCEP were used for input to the SARTA radiative transfer model, specifically designed for AIRS data.

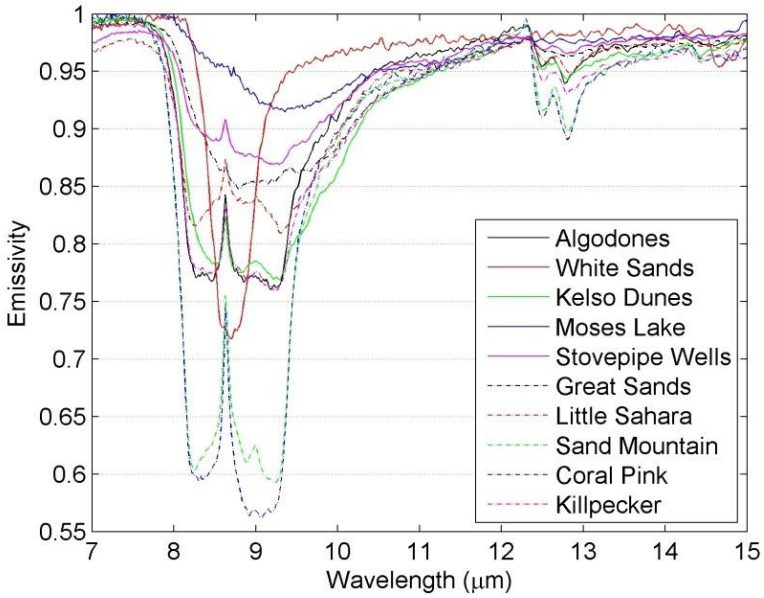

Figure 15. Laboratory-measured emissivity spectra of sand samples collected at 10 pseudo-invariant sand dune validation sites in the southwestern USA. The sites cover a wide range of emissivities in the TIR region.

9 References

Anderson, M.C., Norman, J.M., Mecikalski, J.R., Otkin, J.A., & Kustas, W.P. (2007). A climatological study of evapotranspiration and moisture stress across the continental United States based on thermal remote sensing: 2. Surface moisture climatology. *Journal of Geophysical Research-Atmospheres, 112*, (D11)

Augustine, J.A., DeLuisi J.J., and Long., C.N. (2000). SURFRAD—A national surface radiation budget network for atmospheric research, *Bulletin of the American Meteorological Society 81* (10), pp. 2341–2357.

Baldridge, A.M., Hook, S.J., Grove, C.I., & Rivera, G. (2009). The ASTER Spectral Library Version 2.0. *Remote Sensing of Environment, 114*, (4), 711-715

Bannari, A., Omari, K., Teillet, R.A., & Fedosejevs, G. (2005). Potential of getis statistics to characterize the radiometric uniformity and stability of test sites used for the calibration of earth observation sensors. *IEEE Transactions on Geoscience and Remote Sensing, 43*, (12), 2918-2926

Barducci, A., & Pippi, I. (1996). Temperature and emissivity retrieval from remotely sensed images using the "grey body emissivity" method. *IEEE Transactions on Geoscience and Remote Sensing, 34*, (3), 681-695

Barton, I.J., Zavody, A.M., Obrien, D.M., Cutten, D.R., Saunders, R.W., & Llewellynjones, D.T. (1989). Theoretical Algorithms for Satellite-Derived Sea-Surface Temperatures. *Journal of Geophysical Research-Atmospheres, 94*, (D3), 3365-3375

Becker, F., & Li, Z.L. (1990). Temperature-Independent Spectral Indexes in Thermal Infrared Bands. *Remote Sensing of Environment, 32*, (1), 17-33

Berk, A., Anderson, G.P., Acharya, P.K., Bernstein, L.S., Muratov, L., Lee, J., FOx, M., Adler-Golden, S.M., Chetwynd, J.H., Hoke, M.L., Lockwood, R.B., Gardner, J.A., Cooley, T.W., Borel, C.C., & Lewis, P.E. (2005). MODTRAN^{TM} 5, A Reformulated Atmospheric Band Model with Auxiliary Species and Practical Multiple Scattering Options: Update. S.S. Sylvia & P.E. Lewis (Eds.), *Algorithms and Technologies for Multispectral, Hyperspectral, and Ultraspectral Imagery XI*. Bellingham, WA: Proceedings of SPIE

Brown, O., & Minnett, P. (1999). MODIS infrared sea surface temperature algorithm. *Algorithm Theoretical Basis Document Version 2*, Univ. of Miami, Miami, Fla.

Coll, C., & Caselles, V. (1997). A split-window algorithm for land surface temperature from advanced very high resolution radiometer data: Validation and algorithm comparison. *Journal of Geophysical Research-Atmospheres, 102*, (D14), 16697-16713

Coll, C., Sánchez, J.M., Caselles, V., Valor, E., Niclòs, R., & Galve, J.M. (2005). Validation of ASTER derived surface temperatures and emissivities with ground measurements. *Geophysical Research Abstracts, 7*, 06440

Coll, C., Wan, Z.M., & Galve, J.M. (2009). Temperature-based and radiance-based validations of the V5 MODIS land surface temperature product. *Journal of Geophysical Research-Atmospheres, 114*

Cosnefroy, H.N., Leroy, M., & Briottet, X. (1996). Selection and characterization of Saharan and Arabian desert sites for the calibration of optical satellite sensors. *Remote Sensing of Environment, 58,* (1), 101-114

de Vries, C., Danaher, T., Denham, R., Scarth, P., & Phinn, S. (2007). An operational radiometric calibration procedure for the Landsat sensors based on pseudo-invariant target sites. *Remote Sensing of Environment, 107,* (3), 414-429

Deschamps, P.Y., & Phulpin, T. (1980). Atmospheric Correction of Infrared Measurements of Sea-Surface Temperature Using Channels at 3.7, 11 and 12 Mu-M. *Boundary-Layer Meteorology, 18,* (2), 131-143

French, A.N., Jacob, F., Anderson, M.C., Kustas, W.P., Timmermans, W., Gieske, A., Su, Z., Su, H., McCabe, M.F., Li, F., Prueger, J., & Brunsell, N. (2005). Surface energy fluxes with the Advanced Spaceborne Thermal Emission and Reflection radiometer (ASTER) at the Iowa 2002 SMACEX site (USA) (vol 99, pg 55, 2005). *Remote Sensing of Environment, 99,* (4), 471-471

French, A.N., Schmugge, T.J., Ritchie, J.C., Hsu, A., Jacob, F., & Ogawa, K. (2008). Detecting land cover change at the Jornada Experimental Range, New Mexico with ASTER emissivities. *Remote Sensing of Environment, 112,* (4), 1730-1748

Gillespie, A., Rokugawa, S., Matsunaga, T., Cothern, J.S., Hook, S., & Kahle, A.B. (1998). A temperature and emissivity separation algorithm for Advanced Spaceborne Thermal Emission and Reflection Radiometer (ASTER) images. *IEEE Transactions on Geoscience and Remote Sensing, 36,* (4), 1113-1126

Gillespie, A., Rokugawa, S., Hook, S., Matsunaga, T., & Kahle, A.B. (1999). Temperature/Emissivity Separation Algorithm Theoretical Basis Document, Version 2.4, ASTER TES ATBD, NASA Contract NAS5-31372, 31322 March, 31999

Gustafson, W.T., Gillespie, A.R., & Yamada, G.J. (2006). Revisions to the ASTER temperature/emissivity separation algorithm, *2nd International Symposium on Recent Advances in Quantitative Remote Sensing*. Torrent (Valencia), Spain

Hook, S.J., Dmochowski, J.E., Howard, K.A., Rowan, L.C., Karlstrom, K.E., & Stock, J.M. (2005). Mapping variations in weight percent silica measured from multispectral thermal infrared imagery

- Examples from the Hiller Mountains, Nevada, USA and Tres Virgenes-La Reforma, Baja California Sur, Mexico. *Remote Sensing of Environment, 95,* (3), 273-289

Hook, S.J., Gabell, A.R., Green, A.A., & Kealy, P.S. (1992). A Comparison of Techniques for Extracting Emissivity Information from Thermal Infrared Data for Geologic Studies. *Remote Sensing of Environment, 42,* (2), 123-135

Hook, S.J., Vaughan, R.G., Tonooka, H., & Schladow, S.G. (2007). Absolute radiometric in-flight validation of mid infrared and thermal infrared data from ASTER and MODIS on the terra spacecraft using the Lake Tahoe, CA/NV, USA, automated validation site. *IEEE Transactions on Geoscience and Remote Sensing, 45,* (6), 1798-1807

Hulley, G.C., & Hook, S.J. (2009a). Intercomparison of Versions 4, 4.1 and 5 of the MODIS Land Surface Temperature and Emissivity Products and Validation with Laboratory Measurements of Sand Samples from the Namib Desert, Namibia. *Remote Sensing of Environment, 113*, 1313-1318

Hulley, G.C., & Hook, S.J. (2009b). The North American ASTER Land Surface Emissivity Database (NAALSED) Version 2.0. *Remote Sensing of Environment,* (113), 1967-1975

Hulley, G.C., Hook, S.J., & Baldridge, A.M. (2008). ASTER land surface emissivity database of California and Nevada. *Geophysical Research Letters, 35,* (13), L13401, doi: 13410.11029/12008gl034507

Hulley, G.C., Hook, S.J., & Baldridge, A.M. (2009a). Validation of the North American ASTER Land Surface Emissivity Database (NAALSED) Version 2.0 using Pseudo-Invariant Sand Dune Sites. *Remote Sensing of Environment, 113,* 2224-2233

Hulley, G.C., Hook, S.J., Manning, E., Lee, S.Y., & Fetzer, E.J. (2009b). Validation of the Atmospheric Infrared Sounder (AIRS) Version 5 (v5) Land Surface Emissivity Product over the Namib and Kalahari Deserts. *Journal of Geophysical Research Atmospheres, 114*, D19104

HyspIRI (2008). NASA 2008 HyspIRI Whitepaper and Workshop Report. *Jet Propulsion Laboratory, California Institute of Technology, Pasadena, California,* May 2009

Jimenez-Munoz, J.C., & Sobrino, J.A. (2010). A Single-Channel Algorithm for Land-Surface Temperature Retrieval From ASTER Data. *IEEE Geoscience and Remote Sensing Letters, 7,* (1), 176-179

Jin, M.L., & Dickinson, R.E. (2010). Land surface skin temperature climatology: benefitting from the strengths of satellite observations. *Environmental Research Letters, 5,* (4)

Kealy, M.J., Montgomery, M., & Dovidio, J.F. (1990). Reliability and Predictive-Validity of Contingent Values - Does the Nature of the Good Matter. *Journal of Environmental Economics and Management, 19,* (3), 244-263

Kealy, P.S., & Hook, S. (1993). Separating temperature & emissivity in thermal infrared multispectral scanner data: Implication for recovering land surface temperatures. *IEEE Transactions on Geoscience and Remote Sensing, 31,* (6), 1155-1164

Kneizys, F.X., Abreu, L.W., Anderson, G.P., Chetwynd, J.H., Shettle, E.P., Berk, A., Bernstein, L.S., Robertson, D.C., Acharya, P.K., Rothman, L.A., Selby, J.E.A., Gallery, W.O., & Clough, S.A. (1996). The MODTRAN 2/3 Report & LOWTRAN 7 Model, F19628-91-C-0132, *Phillips Lab.* Hanscom AFB, MA

Li, F.Q., Jackson, T.J., Kustas, W.P., Schmugge, T.J., French, A.N., Cosh, M.H., & Bindlish, R. (2004). Deriving land surface temperature from Landsat 5 and 7 during SMEX02/SMACEX. *Remote Sensing of Environment, 92,* (4), 521-534

Lyon, R. (1965). Analysis of Rocks by Spectral Infrared Emission (8 to 25 microns). *Economic Geology and the Bulletin of the Society of Economic Geologists, 60*, 715-736

Masuda, K., Takashima, T., & Takayama, Y. (1988). Emissivity of Pure and Sea Waters for the Model Sea-Surface in the Infrared Window Regions. *Remote Sensing of Environment, 24,* (2), 313-329

Matsunaga, T. (1994). A temperature-emissivity separation method using an empirical relationship between the mean, the maximum, & the minimum of the thermal infrared emissivity spectrum, in Japanese with English abstract. *Journal Remote Sensing Society Japan, 14,* (2), 230-241

Mira, M., Valor, E., Boluda, R., Caselles, V., & Coll, C. (2007). Influence of soil water content on the thermal infrared emissivity of bare soils: Implication for land surface temperature determination. *Journal of Geophysical Research-Earth Surface, 112,* (F4), F04003

Mushkin, A., & Gillespie, A.R. (2005). Estimating sub-pixel surface roughness using remotely sensed stereoscopic data. *Remote Sensing of Environment, 99,* (1-2), 75-83

NRC (2007). Earth Science and Applications from Space: National Imperatives for the Next Decade and Beyond, 2007. Committee on Earth Science and Applications from Space: A Community Assessment and Strategy for the Future, *National Research Council, National Academies Press. Referred to as the Decadal Survey or NRC 2007.*

Norman, J.M., & Becker, F. (1995). Terminology in Thermal Infrared Remote-Sensing of Natural Surfaces. *Agricultural and Forest Meteorology, 77,* (3-4), 153-166

Ogawa, K., Schmugge, T., & Rokugawa, S. (2006). Observations of the dependence of the thermal infrared emissivity on soil moisture. *Geophysical Research Abstracts, 8*, 04996

Prata, A.J. (1994). Land-Surface Temperatures Derived from the Advanced Very High-Resolution Radiometer and the Along-Track Scanning Radiometer .2. Experimental Results and Validation of Avhrr Algorithms. *Journal of Geophysical Research-Atmospheres, 99,* (D6), 13025-13058

Price, J.C. (1984). Land surface temperature measurements from the split window channels of the NOAA 7 Advanced Very High Resolution Radiometer. *Journal of Geophysical Research, 89,* (D5), 7231-7237

Schmugge, T., & Ogawa, K. (2006). Validation of Emissivity Estimates from ASTER and MODIS Data, *Proceedings of 2006 International Geoscience and Remote Sensing Symposium* (pp. 260-262)

Schmugge, T., Ogawa, K., Jacob, F., French, A., Hsu, A., & Ritchie, J.C. (2003). Validation of Emissivity Estimates from Aster Data *Proceedings of 2003 International Geoscience and Remote Sensing Symposium* (pp. 1873-1875)

Snyder, W.C., Wan, Z., Zhang, Y., & Feng, Y.Z. (1998). Classification-based emissivity for land surface temperature measurement from space. *International Journal of Remote Sensing, 19,* (14), 2753-2774

Teillet, P.M., Fedosejevs, G., Gautier, R.P., & Schowengerdt, R.A. (1998). Uniformity characterization of land test sites used for radiometric calibration of earth observation sensors, *Proc. 20th Can. Symp. Remote Sensing* (pp. 1-4). Calgary, AB, Canada

Tonooka, H. (2005). Accurate atmospheric correction of ASTER thermal infrared imagery using the WVS method. *IEEE Transactions on Geoscience and Remote Sensing, 43,* (12), 2778-2792

Tonooka, H., & Palluconi, F.D. (2005). Validation of ASTER/TIR standard atmospheric correction using water surfaces. *IEEE Transactions on Geoscience and Remote Sensing, 43,* (12), 2769-2777

Vaughan, R.G., Hook, S.J., Calvin, W.M., & Taranik, J.V. (2005). Surface mineral mapping at Steamboat Springs, Nevada, USA, with multi-wavelength thermal infrared images. *Remote Sensing of Environment, 99,* (1-2), 140-158

Wan, Z.M., & Li, Z.L. (1997). A physics-based algorithm for retrieving land-surface emissivity and temperature from EOS/MODIS data. *IEEE Transactions on Geoscience and Remote Sensing, 35,* (4), 980-996

Wan, Z., & Li, Z.L. (2008). Radiance-based validation of the V5 MODIS land-surface temperature product. *International Journal of Remote Sensing, 29,* (17-18), 5373-5395

Wan, Z.M., & Dozier, J. (1996). A generalized split-window algorithm for retrieving land-surface temperature from space. *IEEE Transactions on Geoscience and Remote Sensing, 34,* (4), 892-

905Watson, K. (1992). Spectral Ratio Method for Measuring Emissivity. *Remote Sensing of Environment, 42,* (2), 113-116

Wang W., Liang, S. (2009). Estimation of high-spatial resolution clear-sky longwave downward and net radiation over land surfaces from MODIS data. Remote Sensing of Environment, 113(4), 745-75

Watson, K., Kruse, F.A., & Hummermiller, S. (1990). Thermal Infrared Exploration in the Carlin Trend, Northern Nevada. *Geophysics, 55,* (1), 70-79

Yu, Y., Privette, J.L., & Pinheiro, A.C. (2008). Evaluation of split-window land surface temperature algorithms for generating climate data records. *IEEE Transactions on Geoscience and Remote Sensing, 46,* (1), 179-192